

# AWECS: A Linear Gyrokinetic $\delta f$ Particle-in-Cell Simulation Code for the Study of Alfvénic Instabilities in High- $\beta$ Tokamak Plasmas

Andreas Bierwage<sup>1,\*</sup> and Liu Chen<sup>1,2</sup>

<sup>1</sup> *Department of Physics and Astronomy, University of California, Irvine, CA 92697, U.S.A.*

<sup>2</sup> *Institute for Fusion Theory and Simulation, Zhejiang University, Hangzhou, China*

September 12, 2021

## Abstract

A 1-D linear gyrokinetic code called AWECS is developed to study the kinetic excitation of Alfvénic instabilities in a high- $\beta$  tokamak plasma, with  $\beta$  being the ratio of thermal to magnetic pressure. It is designed to describe physics associated with a broad range of frequencies and wavelengths. For example, AWECS is capable of simulating kinetic ballooning modes, Alfvénic ion-temperature-gradient-driven modes, as well as Alfvén instabilities due to energetic particles. In addition, AWECS may be used to study drift-Alfvén instabilities in the low- $\beta$  regime. Here, the layout of the code and the numerical methods used are described. AWECS is benchmarked against other codes and a convergence study is carried out.

## 1 Introduction

In a tokamak, nested closed toroidal magnetic surfaces are used to confine a high-temperature plasma consisting mainly of ionized Deuterium. Such magnetized plasmas are known to support various kinds of magnetohydrodynamic (MHD) shear Alfvén waves (SAW), the properties of which are determined by the geometry of the magnetic flux surfaces; in particular, the field line curvature and magnetic shear. Resonant and non-resonant interactions between SAWs and plasma particles can lead to excitations of SAW instabilities. These instabilities may, in turn, affect particle confinement. In order to optimize the tokamak geometry and operating conditions for thermonuclear fusion applications, a thorough understanding of SAW physics is crucial. For a review of SAW observations and comparison with theory see, e.g., Ref. [1].

In order to investigate the linear instability of SAWs, a linear gyrokinetic particle-in-cell (PIC) simulation code, called AWECS, is developed. The model equations describe the dynamics local to a field-aligned flux-tube using the so-called ballooning formalism. The equations are valid for a broad range of frequencies and wavelengths, with focus on temperature- and pressure-gradient-driven instabilities, while ignoring modes driven by the gradient of the parallel plasma current. For instance, AWECS allows to study electrostatic and Alfvénic ion-temperature-gradient modes (ESITG and AITG) [2, 3], kinetic ballooning modes (KBM) [4],  $\beta$ -induced Alfvén eigenmodes (BAE) [5], toroidicity-induced Alfvén eigenmodes (TAE) [6],  $\alpha$ -induced toroidal Alfvén eigenmodes ( $\alpha$ TAE) [7], as well as energetic particle modes (EPM) [8]. In addition, AWECS may be used to study drift-Alfvén instabilities in the low- $\beta$  regime [9]. Here,  $\beta = 2\mu_0 P/B_0^2$  is the ratio of thermal to magnetic pressure, and  $\alpha = -q^2 R_0 d\beta/dr$  is the normalized pressure gradient, with  $q$  being the safety factor (a measure for the field line pitch),  $R_0$  the major radius of the torus,  $r$  the minor radial coordinate, and  $B_0$  the field strength at the magnetic axis.

This paper is organized as follows. In Section 2, we describe the physical model and, in Section 3, the numerical methods used to solve the equations. In Sections 4–6, AWECS is benchmarked against other codes, followed by a convergence study in Section 7. Concluding remarks and discussions are given in Section 8.

---

\*abierwag@uci.edu

## 2 Model

In this section, we describe the physical model used. After providing an overview of assumptions made in the derivation, we describe the equilibrium model, followed by the gyrokinetic equation and the electromagnetic field equations. Then the equations are normalized and cast into a form suitable for numerical solution as an initial-value problem. For convenience, in the first part of this section, all time-dependent variables are Laplace-transformed ( $\partial_t \equiv \partial/\partial t \rightarrow -i\omega$ ).

### 2.1 Assumptions and formal ordering

We employ the linear gyrokinetic field equations derived by Zonca & Chen [10]. A reduction similar to that described in Ref. [10] is applied, except that finite-Larmor-radius (FLR) corrections for thermal ions are retained in the present paper. The model is valid for Alfvénic instabilities in a wide range of frequencies  $\omega$  and wave numbers  $k$ , provided that

$$(i) : \omega \ll k_{\parallel} v_{te}, \quad k_{\perp} \rho_{ce} \ll 1, \quad (ii) : \omega \ll \omega_{ci}, \quad (iii) : \omega \lesssim \omega_A; \quad (1)$$

where  $\omega_{cs} = e_s B/m_s$  is the cyclotron frequency and  $\rho_{cs} = v_{\perp}/\omega_{cs}$  the Larmor radius for particle species  $s$  ( $s = e$  for electrons,  $s = i$  for thermal ions, and  $s = E$  for energetic ions). Here,  $k_{\parallel}$  is a short-hand notation for the typical value of  $(\mathbf{B}/B) \cdot \nabla = \partial/\partial l$  in regions where the field perturbation has a significant amplitude. Correspondingly,  $k_{\perp}$  measures the wave number perpendicular to the equilibrium magnetic field  $\mathbf{B}$ . The thermal velocity  $v_{ts}$  is defined as  $T_s = m_s v_{ts}^2$ . The restrictions in Eq. (1) mean that (i) we consider wave dynamics which are adiabatic with respect to electron dynamics and neglect electron-FLR effects (formally:  $m_e \rightarrow 0^+$ ), (ii) the magnetic moment is conserved (no cyclotron resonances), and (iii) the interaction with fast magnetosonic waves is negligible. Although, assumption (i),  $\omega \ll k_{\parallel} v_{te}$ , is applicable only to passing electrons, kinetic effects associated with magnetically trapped electrons are ignored at this stage. Assumption (ii) implies that the only relevant “kinetic effect” is the kinetic compression of ions along the magnetic field, so the particle dynamics are described in terms of the parallel velocity  $v_{\parallel}$  and the position  $l$  along a field line.

In this study, effects associated with the anisotropy of the equilibrium particle distribution  $f_0$  are neglected; thus, we let  $P = P_{\perp} \approx P_{\parallel}$ . Furthermore, since we are dealing with low-frequency waves,  $\omega/k \ll c$ , the displacement current in Ampère’s law is neglected ( $\nabla \times \mathbf{B} \approx \mu_0 \mathbf{j}$ ). As is typical for tokamaks, the plasma is taken to be sufficiently dense to satisfy the quasi-neutrality condition; i.e.,  $k_{\perp} \ll 1/\lambda_{De}$ , with  $\lambda_{De}$  being the electron Debye length.

The equations are linearized by separating the distribution  $\mathcal{F}_s$  (phase-space density) and the electromagnetic fields  $\mathbf{E}_{\text{tot}}$  and  $\mathbf{B}_{\text{tot}}$  into equilibrium and perturbed components,

$$\mathcal{F}_s = f_{0s} + \delta f_s, \quad \mathbf{B}_{\text{tot}} = \nabla \times \mathbf{A}_{\text{tot}} = \mathbf{B} + \delta \mathbf{B}, \quad \mathbf{E}_{\text{tot}} = \delta \mathbf{E} = -\nabla \delta \phi - \partial_t \delta \mathbf{A}; \quad (2)$$

where we have assumed that the equilibrium is static ( $\mathbf{E}_{\text{tot}} = \delta \mathbf{E}$ ). We use the Coulomb gauge  $\nabla \cdot \mathbf{A}_{\text{tot}} = 0$ . Since we consider micro-scale instabilities, the length scales of equilibrium and perturbed quantities are disparate in the direction perpendicular to the magnetic field; i.e.,  $k_{\perp} \gg k_{0\perp}$ . Due to the stabilizing influence of magnetic tension, perturbations tend to be aligned with the magnetic field, so that  $k_{\perp} \gg k_{\parallel}$  and the perturbations have a nearly flute-like structure.

In a tokamak, the toroidal component of the magnetic field is much stronger than the poloidal component, so that  $B \approx B_T$ . In simple toroidal coordinates  $(r, \vartheta, \zeta)$  (minor radius, poloidal/azimuthal angle, toroidal angle),  $B_T$  has the form

$$B_T = B_0/\hat{R}, \quad \text{with } \hat{R} = R/R_0 = 1 + \varepsilon \cos \vartheta. \quad (3)$$

The typical value for the inverse aspect ratio for the flux surface under consideration,  $\varepsilon = r/R_0$ , is taken to be of the order  $\varepsilon \sim 0.1 \cdots 0.3$ , depending on the proximity to the magnetic axis. The scale length of the equilibrium pressure gradient is taken to be of the order  $L_p/R_0 \sim 0.1$ . Using  $\delta \sim L_p/R_0$  as a small expansion parameter, and noting that  $k_{0\perp} \sim L_p^{-1}$ , we adopt the following formal ordering

[10]:<sup>1</sup>

$$\omega/\omega_A \sim \mathcal{O}(\delta^{1/2}); \quad (4a)$$

$$k_{0\parallel}\rho_{ci} \sim k_{0\perp}\rho_{ci} \sim \mathcal{O}(\delta), \quad k_{\parallel}\rho_{ci} \sim \mathcal{O}(\delta), \quad k_{\perp}\rho_{ci} \sim 1; \quad (4b)$$

$$\frac{n_{0E}}{n_{0i}} \sim \mathcal{O}(\delta^{3/2}), \quad \beta_i = \frac{2T_i}{m_i v_{A0}^2} \sim \mathcal{O}(\delta), \quad \beta_E = \frac{2T_E}{m_i v_{A0}^2} \frac{n_{0E}}{n_{0i}} \sim \mathcal{O}(\delta^{3/2}); \quad (4c)$$

where  $v_{A0} = B_0/\sqrt{\mu_0 m_i n_{0i}}$  is the Alfvén velocity. Furthermore, using the disparity between electron and ion mass,  $m_e/m_i \sim \mathcal{O}(\delta^3)$ , and assuming  $T_e/T_i \sim \mathcal{O}(1)$ , we have

$$v_i/v_e \sim j_{0\parallel i}/j_{0\parallel e} \sim k_{\perp}\rho_e \sim \mathcal{O}(\delta^{3/2}) \quad \rightarrow \quad j_{0\parallel} \approx j_{0\parallel e}. \quad (5)$$

Thus, we may assume that the equilibrium current is carried primarily by electrons. From the above orderings (4a)–(4c) it follows that

$$\frac{\omega}{\omega_{ci}} = \frac{\omega}{\omega_{A0}} \frac{v_A}{v_{ti}} k_{\theta}\rho_{ci} \sim \mathcal{O}(\delta^{3/2}).$$

The density and  $\beta$  orderings (4c) imply that

$$T_i/T_E \sim \mathcal{O}(\delta), \quad k_{\perp}\rho_{cE} \sim \mathcal{O}(\delta^{-1/2}).$$

The wave number ordering (4b) implies that [11]

$$i\mathbf{k}_{\perp} \cdot \delta\mathbf{A}/\delta A_{\parallel} \sim \mathcal{O}(\delta).$$

Note that the above constitutes a maximal ordering, chosen to cover a broad range of plasma parameters; more typical values for the normalized wavenumber used in simulations are, for instance,  $k_{\perp}\rho_{ci} \sim 0.1$  and  $k_{\perp}\rho_{cE} \sim 1$ , which corresponds to  $T_i/T_E \sim \mathcal{O}(\delta^2)$ .

## 2.2 Equilibrium model

The separation of temporal and spatial scales described by Eq. (4), in particular,  $\omega \ll \omega_{ci}$  and  $k_0 \sim k_{\parallel} \ll k_{\perp}$ , allow us to average over the rapid gyromotion and apply an eikonal approximation, which simplifies the problem significantly. The eikonal approximation is facilitated by the so-called ballooning transform [12]. The essential physical effects arising in toroidal geometry are then captured by the so-called  $s$ - $\alpha$  model [12].

For the equilibrium distribution, the separation of temporal and spatial scales implies that, at lowest order,  $f_{0s}$  may be taken to be independent of the position along a field line  $l$  and the gyrophase  $\xi$  [11],

$$\partial_l f_{0s} = \partial_{\xi} f_{0s} = 0. \quad (6)$$

Since the field lines cover magnetic surfaces ergodically, Eq. (6) implies that the equilibrium particle density  $n_{0s}$  is a function of the minor radius  $r$  only. The plasma particle distribution is assumed to be an isotropic ( $T_{\perp} = T_{\parallel}$ ) equilibrium, and we usually decompose it as  $f_{0s} = n_{0s}(r)F_{0s}(r, \mathcal{E})$ . Thermal ions and electrons are taken to obey a Maxwellian velocity distribution

$$f_{0s} = n_{0s}(r)F_{Ms}(r, \mathcal{E}), \quad F_{Ms} = [2\pi\mathcal{T}_s(r)]^{-3/2} e^{-\mathcal{E}/\mathcal{T}_s(r)}; \quad (7)$$

where

$$\mathcal{E} = (v_{\perp}^2 + v_{\parallel}^2)/2, \quad \mathcal{T}_s = k_B T_s/m_s.$$

Energetic ions, such as  $\alpha$ -particles from nuclear fusion reactions and injected beam ions, are generally non-Maxwellian and anisotropic. In the present model, isotropicity is assumed for simplicity, while allowing for a non-Maxwellian distribution (e.g., slowing-down distribution).

Due to axisymmetry, the tokamak equilibrium is effectively a 2-D system, with  $\zeta$  being the ignorable coordinate. Taking advantage of the spatial scale separation, an eikonal approximation would allow to decouple the remaining two dimensions to create two simpler 1-D problems; however, its direct

<sup>1</sup>In Ref. [10], the ordering of the perpendicular wave number is  $k_{\perp}\rho_{ci} \sim \mathcal{O}(\delta)$ . Here, larger values are allowed and FLR corrections will be included.

application is infeasible because the magnetic shear severely distorts the flux tubes, while all physical quantities must be  $2\pi$ -periodic in  $\vartheta$  and  $\zeta$ . The periodicity constraint is eliminated by the ballooning transform, which maps a flux tube of the periodic physical system onto a non-periodic covering space, with the new coordinate being the ballooning angle  $\theta \in (-\infty, \infty)$ . The physical solution is reconstructed from the solutions on the infinite domain by linear superposition. Formally, the ballooning transform in an axisymmetric configuration can be written as [12]

$$\delta\phi(r, \vartheta) = \frac{1}{2\pi} \sum_{m=-\infty}^{\infty} e^{-im\vartheta} \int_{-\infty}^{\infty} d\theta e^{-i\theta(nq-m)} \delta\hat{\phi}(r, \theta) = \sum_{p=-\infty}^{\infty} \delta\hat{\phi}(r, \vartheta + 2\pi p); \quad (8)$$

where  $m$  is the poloidal and  $n$  the toroidal mode number. The transform is valid for short-wavelength modes ( $nq \gg 1$ ). The dependence on  $r$  is then separated as

$$\delta\hat{\phi}(r, \theta) = \delta\hat{\Phi}(\theta)W(r)e^{iS},$$

where  $S$  is the eikonal (rapidly varying with  $r$ ) and  $W$  the slowly varying radial envelope.

In order to proceed further, one has to construct a local model for the MHD equilibrium. A popular choice is the  $s$ - $\alpha$  model by Connor, Hastie and Taylor (CHT) [12], where we may write  $\delta\hat{\phi}(r, \theta) = \delta\hat{\Phi}(\theta)e^{ik_r r}$ . In the simple case of a cylindrical tokamak, the radial wave number is  $k_r = -k_\vartheta s(\theta - \theta_k)$ , where  $s = (r/q)dq/dr$  is the global magnetic shear,  $\theta_k \propto k_{0\perp}$  describes the slowly-varying radial WKB envelope, and  $k_\vartheta = nq/r$  is the poloidal wave number. In toroidal geometry, the thermal pressure modifies the flux surfaces and, thus, imposes a poloidal modulation on the magnetic shear. The CHT  $s$ - $\alpha$  equilibrium model retains the lowest-order effect by assuming that the toroidal magnetic flux surfaces maintain a circular poloidal cross-section while undergoing an outward shift (Shafranov shift). In this case, the gradient and Laplacian operators applied to perturbed fields, and the magnetic curvature drift, have the following form:

$$-\frac{\partial_r}{k_\vartheta} \rightarrow \frac{k_r}{k_\vartheta} = s(\theta - \theta_k) - \alpha \sin \theta \equiv h(\theta), \quad (9a)$$

$$-\frac{\nabla_\perp^2}{k_\vartheta^2} \rightarrow \frac{k_\perp^2}{k_\vartheta^2} = 1 + \frac{k_r^2}{k_\vartheta^2} = 1 + h^2(\theta) \equiv f(\theta); \quad (9b)$$

$$\Omega_\kappa = \mathbf{k}_\perp \cdot (\hat{\mathbf{b}} \times \boldsymbol{\kappa}) = \frac{k_\vartheta}{R(\theta)}g(\theta), \quad g \equiv \cos \theta + h(\theta) \sin \theta, \quad (9c)$$

so that  $k_\perp = k_\vartheta \sqrt{f}$  and the local magnetic shear is  $\partial_\theta h = s - \alpha \cos(\theta)$ . Here,  $\hat{\mathbf{b}} = \mathbf{B}/B$  and  $\boldsymbol{\kappa} = \hat{\mathbf{b}} \cdot \nabla \hat{\mathbf{b}}$  is the field line curvature vector. In this model, the equilibrium is completely described in terms of two parameters: the flux-surface-averaged magnetic shear  $s$  and the normalized pressure gradient  $\alpha$ .

Since the CHT  $s$ - $\alpha$  model is derived for the low- $\beta$ , large-aspect-ratio limit,<sup>2</sup> its application in a study of high- $\beta$  instabilities in tokamak plasmas with  $\varepsilon \gtrsim 0.1$  is somewhat ambiguous. To justify its use, it is argued that it does capture essential effects of toroidal geometry and high  $\beta$ ; namely, toroidal curvature and modulation of the magnetic shear. The presence of these features physically distinguishes a toroidal plasma from a cylindrical or slab geometry. On the other hand, higher-order toroidal effects ignored by the  $s$ - $\alpha$  model (such as elliptic and triangular deformation of the flux surfaces) merely modify the lowest-order results; for instance, by adding further frequency gaps and corresponding Alfvén eigenmodes. Thus, the  $s$ - $\alpha$  model is thought to be a convenient and powerful tool for basic studies of the qualitative features of low- and high- $\beta$  tokamak instabilities.

### 2.3 Gyrokinetic equation

The evolution of the particle distribution  $\mathcal{F}_s$  is chosen to be governed by the Vlasov equation; i.e., the ensemble-averaged phase-space continuity equation in the absence of collisions. For a high-temperature tokamak plasma, where electromagnetic forces dominate, the Vlasov equation reads

$$\left[ \frac{\partial}{\partial t} + \mathbf{v} \cdot \nabla + \frac{e_s}{m_s} (\mathbf{E} + \mathbf{v} \times \mathbf{B}) \cdot \frac{\partial}{\partial \mathbf{v}} \right] \mathcal{F}_s = 0. \quad (10)$$

<sup>2</sup>For a detailed derivation of the CHT  $s$ - $\alpha$  model see, e.g., Ref. [30].

Transformation into guiding center coordinates, linearization, and application of the approximations and orderings outlined in Section 2.1 yields the collisionless linear gyrokinetic equation (GKE) as derived by Antonsen & Lane [11]. Here, we adopt the notation used by Chen & Hasegawa (CH91) [13] and neglect anisotropic contributions due to  $\partial_\mu f_{0s}$ , where  $\mu = v_\perp^2/(2B)$  is the magnetic moment. The fast gyromotion and the electron response to the parallel electric field  $\delta E_\parallel = \partial_l(\delta\psi - \delta\phi)$  are eliminated through the substitution

$$\delta f_s = \frac{e_s}{m_s} [(\omega \partial_\mathcal{E} f_{0s})(\delta\phi - J_0^2 \delta\psi) - (\hat{\omega}_{*s} f_{0s}) J_0^2 \delta\psi] + J_0 \delta K_s^{\text{CH91}}; \quad (11)$$

where

$$\begin{aligned} \mathcal{E} &= v_\perp^2/2 + v_\parallel^2/2, \\ \partial_l \delta\psi &= i\omega \delta A_\parallel \quad (\text{with Coulomb gauge}), \\ \hat{\omega}_{*s} &= \omega_{cs}^{-1} (\mathbf{k}_\perp \times \hat{\mathbf{b}}) \cdot \nabla_g, \end{aligned}$$

and  $\nabla_g$  is the Laplacian in guiding center coordinates. Defining  $\delta G_s \equiv \omega \delta K_s^{\text{CH91}}$ ,  $\delta u = \omega(\delta\phi - \delta\psi)$ , and applying the gyroaverage, one obtains

$$[v_\parallel \partial_l - i(\omega - \omega_{ds})] \delta G_s = i \frac{e_s}{m_s} (\hat{Q} f_{0s}) (\delta S_{1s} - i\hat{\sigma} \delta S_{2s}); \quad (12)$$

with the source terms

$$\delta S_{1s} = J_{0s} \delta u + \omega_{ds} J_{0s} \delta\psi + \frac{v_\perp}{k_\perp} J_{1s} \omega \delta B_\parallel, \quad \delta S_{2s} = -|v_\parallel| (\partial_l \lambda) J_1 \delta\psi; \quad (13)$$

where  $J_i(\lambda_s)$  is the Bessel function of  $i$ -th order,  $\lambda_s = k_\perp v_\perp / \omega_{cs}$ , and  $\hat{\sigma} = v_\parallel / |v_\parallel|$ . The magnetic drift frequency is

$$\omega_{ds} = \Omega_\kappa v_\parallel^2 / \omega_{cs} + \Omega_B \mu B / \omega_{cs} = \Omega_\kappa (v_\parallel^2 + \mu B) / \omega_{cs} + \Omega_p \mu B / \omega_{cs},$$

with

$$\begin{aligned} \Omega_\kappa &= \mathbf{k}_\perp \cdot (\hat{\mathbf{b}} \times \boldsymbol{\kappa}), & \Omega_B &= \mathbf{k}_\perp \cdot (\hat{\mathbf{b}} \times \nabla \ln B) \\ \Omega_p &= -(\mu_0 / B^2) \mathbf{k}_\perp \cdot (\hat{\mathbf{b}} \times \nabla P). \end{aligned}$$

The phase-space-gradient operator  $\hat{Q} = \omega \partial_\mathcal{E} + \hat{\omega}_{*s}$  may be written as

$$\hat{Q} \rightarrow Q = (\omega_{*s}^T - \omega \Theta_s) / T_s,$$

where

$$\omega_{*s}^T = -\omega_{*s} L_{ns} \partial_r \ln f_{0s} \xrightarrow{F_M} \omega_{*s} \left[ 1 + \eta_s \left( \frac{\mathcal{E}}{\mathcal{T}_s} - \frac{3}{2} \right) \right], \quad \Theta_s = -\mathcal{T}_s \partial_\mathcal{E} \ln f_{0s} \xrightarrow{F_M} 1. \quad (14)$$

Here,

$$\omega_{*s} = \frac{k_\vartheta \mathcal{T}_s}{\omega_{c0s} L_{ns}}, \quad L_{ns}^{-1} = -\frac{n'_{0s}}{n_{0s}}, \quad \eta_s = \frac{\mathcal{T}'_s / \mathcal{T}_s}{n'_{0s} / n_{0s}},$$

and the prime denotes a radial derivative. Note that we have used the sign convention  $\hat{\boldsymbol{\zeta}} \cdot \hat{\mathbf{b}} < 0$ , so that

$$(\mathbf{k}_\perp \times \hat{\mathbf{b}}) \cdot \nabla_g \approx -k_\vartheta \partial_r.$$

Finally, application of the ballooning transform ( $qR_0 \partial_l = \partial_\vartheta \rightarrow \partial_\theta$ ) and the CHT  $s$ - $\alpha$  model yields

$$\left[ \frac{v_\parallel}{qR_0} \partial_\theta - i(\omega - \omega_{ds}) \right] \delta G_s = i \frac{e_s f_{0s}}{m_s \mathcal{T}_s} (\omega_{*s}^T - \omega \Theta_s) (\delta S_{1s} - i\hat{\sigma} \delta S_{2s}); \quad (15)$$

where the coefficients in the magnetic drift frequency  $\omega_{ds}$  are given by

$$\Omega_\kappa(\theta) = \frac{k_\vartheta}{R(\theta)} g(\theta), \quad \Omega_p = -\frac{k_\vartheta \alpha}{2q^2 R(\theta) \hat{B}^2(\theta)}. \quad (16)$$

For passing electrons, Eq. (15) is dominated by the  $v_\parallel \partial_\theta$  term alone, which allows us to set  $\delta G_{e,\text{pass}} = 0$ . As mentioned above, in the present work, we ignore trapped-electron effects and set  $\delta G_{e,\text{trap}} = 0$ . Thus, Eq. (15) is solved only for ion species, while electrons are treated as a massless fluid.

## 2.4 Electromagnetic field equations

The evolution of the electromagnetic fields is governed by Maxwell's equations. We adopt the field equations as derived by Zonca & Chen [10], including terms containing  $\partial_\theta \lambda_s$  and neglecting anisotropic contributions due to  $\partial_\mu f_{0s}$ . After application of the ballooning transform, the equations read

$$0 = \frac{k_\vartheta^2}{(qR_0)^2} \frac{\partial}{\partial \theta} \left( f \frac{\partial \delta \psi}{\partial \theta} \right) - \mu_0 \sum_s \left\langle \frac{e^2}{m} (1 - J_0^2) Q f_0 \right\rangle_s \omega \delta \phi - \Omega_p [(\Omega_p + 2\Omega_\kappa) \delta \psi + \omega \delta B_\parallel] \\ - \mu_0 \sum_s \left\langle \frac{e^2}{m} \omega_d (1 - J_0^2) Q f_0 \right\rangle_s \delta \psi - \frac{\mu_0}{B} \sum_s \left\langle e \mu B \left( 1 - \frac{2J_1}{\lambda} J_0 \right) Q f_0 \right\rangle_s \omega \delta B_\parallel \\ - \mu_0 \sum_s \langle e \omega_d J_0 \delta G \rangle_s + i \mu_0 \sum_s \left\langle e \frac{v_\parallel}{qR_0} (\partial_\theta \lambda) J_1 \delta G \right\rangle_s, \quad (17a)$$

$$0 = \sum_s \langle e J_0 \delta G \rangle_s + \sum_s \left\langle \frac{e^2}{m} \partial_\varepsilon f_0 \right\rangle_s \omega (\delta \phi - \delta \psi) + \sum_s \left\langle \frac{e^2}{m} (1 - J_0^2) Q f_0 \right\rangle_s \delta \psi, \quad (17b)$$

$$0 = \omega \delta B_\parallel + \Omega_p \delta \psi + \sum_s \left\langle e \mu B \left( 1 - \frac{2J_1}{\lambda} J_0 \right) Q f_0 \right\rangle_s \delta \psi + \frac{\mu_0}{B} \sum_s \left\langle m \mu B \frac{2J_1}{\lambda} \delta G \right\rangle_s; \quad (17c)$$

where

$$Q = (\omega_{*s}^T - \omega \Theta_s) / \mathcal{T}_s, \quad \langle \dots \rangle_s = \int d^3 v.$$

Equation (17a) is the so-called vorticity equation and is obtained by substituting the parallel Ampère's law into the continuity equation, which, in turn, is obtained by taking the zeroth-order velocity moment of the gyrokinetic equation (15). Equation (17b) is the quasi-neutrality condition, which originally read

$$\sum_s \langle e_s f_{0s} \rangle = 0,$$

and Eq. (17c) is the perpendicular Ampère's law.

## 2.5 Definitions and normalization

The following dimensionless parameters are used in the present work:

$$\varepsilon = \frac{r}{R_0}, \quad \varepsilon_{ns} = \frac{L_{ns}}{R_0} = \varepsilon \frac{d \ln r}{d \ln n_{0s}}, \quad \varepsilon_{ps} = \varepsilon \frac{d \ln r}{d \ln P_s}, \\ \eta_s = \frac{d \ln \mathcal{T}_s}{d \ln n_{0s}}, \quad \tau_{ss'}^T = \frac{m_s \mathcal{T}_s}{m_{s'} \mathcal{T}_{s'}}, \quad \tau_{ss'}^n = \frac{Z_s n_{0s}}{Z_{s'} n_{0s'}}, \quad Z_s = -\frac{e_s}{e_e}, \quad (18) \\ M_s = \frac{m_s}{m_i}, \quad \hat{k}_s = \frac{k_\vartheta \mathcal{T}_s^{1/2}}{\omega_{cs}}, \quad b_s = f \hat{k}_s^2, \quad \lambda_s = \sqrt{f} \frac{k_\vartheta v_\perp}{\omega_{cs}}.$$

Since we are dealing with a quasi-neutral Deuterium plasma ( $Z_i = 1$ ) containing only a sparse population of energetic particles, we have  $\varepsilon_{ni} = \varepsilon_{ne}$ . Note that  $\varepsilon_{ns} = \varepsilon_{ps}(1 + \eta_s)$ .

The equations are normalized in two steps. In the first step, we let

$$\hat{v} = \frac{v}{v_{A0}}, \quad \hat{\omega} = \frac{\omega}{\omega_{A0}}, \quad \hat{\Omega}_{\kappa s} = \frac{v_{A0}^2 \Omega_\kappa}{\omega_{A0} \omega_{cs}} = \frac{q \hat{k}_{0s} g(\theta)}{\mathcal{T}_s^{1/2}}, \\ \hat{\Omega}_{ps} = \frac{v_{A0}^2 \Omega_p}{\omega_{A0} \omega_{cs}} = -\frac{\alpha \hat{k}_{0s}}{2q \mathcal{T}_s^{1/2} \hat{B}^2(\theta)}, \quad \left\{ \begin{array}{c} \delta \hat{G}_s \\ \hat{F}_{Ms} \end{array} \right\} = \frac{v_{A0}^3}{n_{0s}} \left\{ \begin{array}{c} \delta G_s \\ F_{Ms} \end{array} \right\}, \quad (19) \\ \delta \Psi_e = \frac{e_e \delta \psi}{m_e \mathcal{T}_e}, \quad \delta U_e = \frac{e_e}{m_e \mathcal{T}_e} \frac{\delta u}{\omega_{A0}}, \quad \delta C_e = \frac{e_e}{m_e \mathcal{T}_e} \frac{v_{A0}^2 \omega \delta B_\parallel}{\omega_{A0} \omega_{ci}};$$

where

$$v_{A0} = v_A / \hat{B}, \quad \omega_{A0} = v_{A0} / (qR_0), \quad \hat{B} = B / B_0 = R_0 / R.$$

Note that  $2\hat{\mathcal{T}}_i = \beta_i = 2\mu_0 P_i / B_0^2$  and  $\hat{k}_s = \hat{k}_{0s} / \hat{B}$ . In the second step, we let

$$\begin{aligned} \tilde{v}^2 &= \frac{\hat{v}^2}{\hat{\mathcal{T}}_s}, & \tilde{\Omega}_{\kappa s} &= \hat{\mathcal{T}}_s \hat{\Omega}_{\kappa s}, & \tilde{\Omega}_{ps} &= \hat{\mathcal{T}}_s \hat{\Omega}_{ps}, \\ \delta\tilde{C}_e &= \hat{\mathcal{T}}_i \delta C_e, & \left\{ \begin{array}{c} \delta\tilde{G}_s \\ \tilde{F}_{Ms} \end{array} \right\} &= \hat{\mathcal{T}}_s^{3/2} \left\{ \begin{array}{c} \delta\hat{G}_s \\ \hat{F}_{Ms} \end{array} \right\}; \end{aligned} \quad (20)$$

so that the normalized drift frequencies become

$$\begin{aligned} \tilde{\omega}_{*s} &= \frac{q\hat{k}_{0s}\hat{\mathcal{T}}_s^{1/2}}{\varepsilon_{ns}}, & \tilde{\omega}_{ds} &= \tilde{\Omega}_{\kappa s} (v_{\parallel}^2 + \mu B) + \tilde{\Omega}_{ps} \mu B, \\ \tilde{\Omega}_{\kappa s} &= q\hat{k}_{0s}\hat{\mathcal{T}}_s^{1/2}g(\theta), & \tilde{\Omega}_{ps} &= -\frac{\alpha\hat{k}_{0s}\hat{\mathcal{T}}_s^{1/2}}{2q\hat{B}^2(\theta)}. \end{aligned} \quad (21)$$

Furthermore, we have

$$\lambda_s = \sqrt{\tilde{b}_s} \tilde{v}_{\perp}, \quad \Theta_s = -\partial_{\tilde{\mathcal{E}}} \ln f_{0s}, \quad \tilde{\omega}_{*s}^T(F_M) = \tilde{\omega}_{*s} [1 + \eta_s (\tilde{\mathcal{E}} - 3/2)].$$

In the following, for simplicity, we will omit the tildes and hats indicating normalized quantities, except for  $\hat{B}$  and  $\hat{k}_s$ .

The second normalization is motivated as follows. First, the values of input parameters determining the velocity space domain size to be sampled numerically become independent of the species' temperature and may, thus, be kept constant once a set of suitable values has been determined. Second, we prevent  $\Omega_{\kappa i}$  and  $\Omega_{pi}$  from diverging, and  $F_{Mi}$  from collapsing into a Dirac  $\delta$  distribution in the limit  $\mathcal{T}_i \rightarrow 0$ .

Note that, in AWECS,  $\mathcal{T}_i$  must remain finite; the case  $\mathcal{T}_i = 0$  can only be realized if  $\mathcal{T}_i^{1/2}$  is included in the time normalization, which is only done in an electrostatic version of the code (see Section 4). The wave number  $\hat{k}_s$  is taken to be parametrically independent of  $\mathcal{T}_s$ , which implies that  $k_{\theta} \propto \mathcal{T}_s^{-1/2}$ .

All moments in Eq. (17) involving the Maxwellian distribution,  $\langle \dots F_{Ms} \rangle$ , can be evaluated analytically, which gives rise to the following quantities:

$$\begin{aligned} \Gamma_{0s} &= e^{-b_s} I_0(b_s), & \Delta_{0s} &= 1 - \frac{I_{1s}}{I_{0s}}, & \Delta_{1s} &= 1 + \frac{b_s}{2} \left( \frac{I_{1s}}{I_{0s}} - 1 \right), \\ \Delta_{2s} &= \frac{7}{4} + \frac{b_s}{2} \left( \frac{5}{2} \frac{I_{1s}}{I_{0s}} - 3 \right) - \frac{b_s^2}{2} \left( \frac{I_{1s}}{I_{0s}} - 1 \right), & \Delta_{3s} &= 1 + \frac{b_s}{2} \left( 3 \frac{I_{1s}}{I_{0s}} - 4 \right) - b_s^2 \left( \frac{I_{1s}}{I_{0s}} - 1 \right), \\ \Upsilon_{0s} &= \Delta_{0s} + \eta_s (1 - 2b_s \Delta_{0s}) = \Delta_{0s} + 2(\Upsilon_{1s} - 1) + \eta_s, & \Upsilon_{1s} &= 1 + \eta_s b_s \left( \frac{I_{1s}}{I_{0s}} - 1 \right), \\ \Upsilon_{2\kappa s} &= \Delta_{1s} + \eta_s \Delta_{3s}, & \Upsilon_{2ps} &= \left( \Delta_{1s} - \frac{1}{2} \right) + \eta_s \left[ \Delta_{3s} - \left( \Delta_{1s} - \frac{1}{2} \right) \right]; \end{aligned} \quad (22)$$

with  $I_i$  being the modified Bessel function  $i$ -th order. These quantities are used in the next section.

## 2.6 Final form of the equations

In this section, we write down the normalized equations in a form suitable for numerical solution as an initial value problem. In the following, we denote  $\partial_{\theta} f$  by  $f'$  and the Laplace transform in time is undone. For energetic ions, the normalized velocity space integrals are given in both the general form valid for any equilibrium distribution,  $F_{0s} = f_{0s}/n_{0s}$ , and the form for a Maxwellian ( $F_{0s} = F_{Ms}$ ).

### Marker motion and gyrokinetic equation

The evolution of the position  $\theta_j$  of a particle labeled  $j$  is governed by the equation

$$d_t \theta_j = \mathcal{T}_s^{1/2} v_{\parallel j}(\theta_j). \quad (23)$$

In order to eliminate  $\omega \leftrightarrow i\partial_t$  on the right-hand side of the GKE, the slow response of the ions is split as follows:<sup>3</sup>

$$\delta G_s = \delta g_s + \Theta_s F_{0s} (\delta S_{1s} - i\hat{\sigma}\delta S_{2s}), \quad (24)$$

which yields (for  $s \neq e$ )

$$\mathcal{L}_0 \delta g_s = -i\omega_{ds} \delta g_s + iF_{0s} [(\omega_{*s}^T - \Theta_s \omega_{ds}) (\delta S_{1s} - i\hat{\sigma}\delta S_{2s}) + \Theta_s \delta \Lambda_{1s} + \Theta_s \delta \Lambda_{2s}]. \quad (25)$$

Here,  $\mathcal{L}_0 = \partial_t + \mathcal{T}_s^{1/2} v_{\parallel} \partial_{\theta}$  is the propagator and the source terms are

$$\delta S_{1s} = J_{0s} \delta U_s + \omega_{ds} J_{0s} \delta \Psi_s + \frac{\tau_{si}^T v_{\perp}^2}{Z_s \lambda_s} J_{1s} \delta C_s, \quad \delta S_{2s} = -\mathcal{T}_s^{1/2} |v_{\parallel}| \lambda'_s J_{1s} \delta \Psi_s. \quad (26)$$

The derivatives  $\delta \Lambda_{1s} = i v_{\parallel} \partial_{\theta} \delta S_{1s}$  and  $\delta \Lambda_{2s} = |v_{\parallel}| \partial_{\theta} \delta S_{2s}$  are given by

$$\begin{aligned} \delta \Lambda_{1s} = & i \mathcal{T}_s^{1/2} v_{\parallel} \left\{ J_0 \delta U' + \omega_d J_0 \delta \Psi' + \omega'_d J_0 \delta \Psi + \frac{\tau_{si}^T v_{\perp}^2}{Z \lambda} J_1 \delta C' + \frac{\hat{B}'}{\hat{B}} \frac{\tau_{si}^T v_{\perp}^2}{Z \lambda} J_1 \delta C \right\}_s \\ & + i \mathcal{T}_s^{1/2} v_{\parallel} \lambda'_s \left\{ -J_1 \delta U - \omega_d J_1 \delta \Psi + \frac{\tau_{si}^T v_{\perp}^2}{Z \lambda} \left( J_0 - \frac{2J_1}{\lambda} \right) \delta C \right\}_s, \end{aligned} \quad (27a)$$

$$\delta \Lambda_{2s} = T_s \mu B \frac{B'}{B} \lambda'_s J_{1s} \delta \Psi_s - \mathcal{T}_s v_{\parallel}^2 \left\{ \lambda' J_1 \delta \Psi' + \lambda \left[ \frac{\lambda''}{\lambda} - \left( \frac{\lambda'}{\lambda} \right)^2 \right] J_1 \delta \Psi + (\lambda')^2 J_0 \delta \Psi \right\}_s; \quad (27b)$$

where  $\delta S_s = -Z_s \tau_{es}^T \delta S_e$  (similarly for  $\delta \Psi_s$ ,  $\delta U_s$ , and  $\delta C_s$ ),  $J_i = J_i(\lambda)$ , and  $\lambda_s = \sqrt{\mathcal{F}} \hat{k}_s v_{\perp}$ . The derivatives of  $\lambda_s$  and  $\omega_{ds}$  with respect to  $\theta$  are

$$\begin{aligned} \lambda'_s / \lambda &= h(s - \alpha \cos \theta) / f - \hat{B}' / (2\hat{B}), \\ \lambda''_s / \lambda_s - (\lambda' / \lambda)^2 &= [h\alpha \sin \theta + (2 - f)(h')^2] / f^2 + \hat{B}'' / (2\hat{B}) - (\hat{B}' / \hat{B})^2 / 2, \\ \omega'_{ds} &= (\Omega_{\kappa s} / g) [h \cos \theta + (h' - 1) \sin \theta] (v_{\parallel}^2 + \mu B) - (\Omega_{\kappa s} + \Omega_{ps}) \mu B (\hat{B}' / \hat{B}). \end{aligned} \quad (28)$$

## Vorticity equation

The vorticity equation is a second-order differential equation in time  $t$ . Collecting all time derivatives in an auxiliary field  $\delta E_e$ , we obtain two first-order equations: the continuity equation<sup>4</sup>

$$\begin{aligned} \partial_t \delta E_e = & \hat{k}_{0i}^2 [f \delta \Psi''_e + 2hh' \delta \Psi'_e] - [\omega_{*i} (1 - \Gamma_{0i} \Upsilon_{1i}) + H_{EU}] \delta U_e \\ & + \omega_{*i} [2\tau_{ei}^T (1 + \eta_e) \Omega_{\kappa i} + \tau_{ei}^T (1 + \eta_e) \Omega_{pi} + 2\Omega_{\kappa i} \Gamma_{0i} \Upsilon_{2\kappa i} + 2\Omega_{pi} \Gamma_{0i} \Upsilon_{2pi}] \delta \Psi_e \\ & + H_{E\Psi} \delta \Psi_e + \omega_{*i} [\tau_{ei}^T (1 + \eta_e) + \Gamma_{0i} \Upsilon_{0i}] \delta C_e + H_{EC} \delta C_e \\ & + \frac{1}{\tau_{ei}^T} \langle \omega_d J_0 \delta G \rangle_i + \frac{\tau_{Ei}^n}{\tau_{ei}^T} \langle \omega_d J_0 \delta G \rangle_E - i \frac{\mathcal{T}_i^{1/2}}{\tau_{ei}^T} \langle v_{\parallel} \lambda' J_1 \delta G \rangle_i - i \frac{\mathcal{T}_E^{1/2} \tau_{Ei}^n}{\tau_{ei}^T} \langle v_{\parallel} \lambda' J_1 \delta G \rangle_E, \end{aligned} \quad (29)$$

and the parallel Ampère's law (which now defines  $\delta E_e$ )

$$\begin{aligned} A_{\omega} \partial_t \delta \Psi_e = & i [2(\Omega_{\kappa i} + \Omega_{pi})(1 - \Gamma_{0i} \Delta_{1i}) - \Omega_{pi}(1 - \Gamma_{0i}) - \omega_{*i}(1 - \Gamma_{0i} \Upsilon_{1i})] \delta \Psi_e \\ & + i H_{\Psi\Psi} \delta \Psi_e + \delta E_e + i A_{\omega} \delta U_e + i(1 - \Gamma_{0i} \Delta_{0i}) \delta C_e + i H_{\Psi C} \delta C_e; \end{aligned} \quad (30)$$

<sup>3</sup>Before normalization, this transformation reads  $\delta G_s = \delta g_s - \frac{e_s}{m_s} (\partial_t f_{0s}) (\delta S_{1s} - i\hat{\sigma}\delta S_{2s})$ .

<sup>4</sup>Note that we have combined the drift-kinetic and FLR components of the ballooning terms ( $\propto \delta \Psi_e, \delta C_e$ ) which are separate in Eq. (17a).



where  $A_\omega = (1 - \Gamma_{0i}) + H_\omega$ , and the energetic particle terms are

$$\begin{aligned}
H_{EU} &= Z_E \tau_{Ei}^n \tau_{iE}^T \langle (1 - J_0^2) \omega_*^T F_0 \rangle_E \xrightarrow{F_M} Z_E \tau_{Ei}^n \tau_{iE}^T \omega_{*E} (1 - \Gamma_{0E} \Upsilon_{1E}), \\
H_{E\Psi} &= Z_E \tau_{Ei}^n \tau_{iE}^T \langle J_0^2 \omega_d \omega_*^T F_0 \rangle_E \xrightarrow{F_M} 2 \tau_{Ei}^n \omega_{*E} [\Omega_{\kappa i} \Gamma_{0E} \Upsilon_{2\kappa E} + \Omega_{pi} \Gamma_{0i} \Upsilon_{2pE}], \\
H_{EC} &= \tau_{Ei}^n \left\langle \mu B \frac{2J_1 J_0}{\lambda} \omega_*^T F_0 \right\rangle_E \xrightarrow{F_M} \tau_{Ei}^n \omega_{*E} \Gamma_{0E} \Upsilon_{0E}, \\
H_{\Psi\Psi} &= Z_E \tau_{Ei}^n \tau_{iE}^T \langle (1 - J_0^2) \omega_d \Theta_s F_0 \rangle_E - H_{EU}, \\
&\xrightarrow{F_M} 2 \tau_{Ei}^n (\Omega_{\kappa i} + \Omega_{pi}) (1 - \Gamma_{0E} \Delta_{1E}) - \tau_{Ei}^n \Omega_{pi} (1 - \Gamma_{0E}) - H_{EU} (F_0 = F_M), \\
H_{\Psi C} &= \tau_{Ei}^n \left\langle \mu B \left( 1 - \frac{2J_1 J_0}{\lambda} \right) \Theta_s F_0 \right\rangle_E \xrightarrow{F_M} \tau_{Ei}^n (1 - \Gamma_{0E} \Delta_{0E}), \\
H_\omega &= Z_E \tau_{Ei}^n \tau_{iE}^T \langle (1 - J_0^2) \Theta_s F_0 \rangle_E \xrightarrow{F_M} Z_E \tau_{Ei}^n \tau_{iE}^T (1 - \Gamma_{0E}).
\end{aligned} \tag{31}$$

The moments of the transformation  $\delta G \rightarrow \delta g$  are:

$$\begin{aligned}
\frac{\langle \omega_d J_0 (\delta G - \delta g) \rangle_s}{\tau_{ei}^T} &= -Z_s \tau_{is}^T [\langle \omega_d J_0^2 \Theta F_0 \rangle_s \delta U_e + \langle \omega_d^2 J_0^2 \Theta F_0 \rangle_s \delta \Psi_e] - \left\langle \omega_d \mu B \frac{2J_1 J_0}{\lambda} \Theta F_0 \right\rangle_s \delta C_e \\
&\xrightarrow{F_M} -\Gamma_{0s} [2(\Omega_{\kappa i} + \Omega_{pi}) \Delta_{1s} - \Omega_{pi}] \delta U_e \\
&\quad - 2 \frac{\tau_{si}^T}{Z_s} \Gamma_{0s} \left[ (\Omega_{\kappa i} + \Omega_{pi})^2 \Delta_{3s} + 2\Omega_{\kappa i} (\Omega_{\kappa i} + \Omega_{pi}) \left( \Delta_{1s} - \frac{1}{2} \right) + \frac{3}{2} \Omega_{\kappa i}^2 \right] \delta \Psi_e \\
&\quad - \frac{\tau_{si}^T}{Z_s} \Gamma_{0s} [\Omega_{\kappa i} (1 + 2\Delta_{0s} - 2b_i \Delta_{0s}) + \Omega_{pi} (1 + \Delta_{0s} - 2b_i \Delta_{0s})] \delta C_e, \\
-i \frac{\sqrt{\mathcal{T}_s}}{\tau_{ei}^T} \langle v_{\parallel} \lambda' J_1 (\delta G - \delta g) \rangle_s &= -\frac{Z_s}{M_s} \mathcal{T}_i \left( \frac{\lambda'_s}{\lambda_s} \right)^2 \langle v_{\parallel}^2 \lambda^2 J_1^2 \Theta F_0 \rangle_s \delta \Psi_e \\
&\xrightarrow{F_M} -2 \frac{Z_s}{M_s} \mathcal{T}_i \left( \frac{\lambda'_s}{\lambda_s} \right)^2 b_s^2 \Gamma_{0s} \Delta_{0s} \delta \Psi_e.
\end{aligned} \tag{32}$$

In the low- $\beta$  limit we may set

$$\delta B_{\parallel} = \Omega_p = 0.$$

By neglecting the energetic ion terms we then recover the model used by Zhao & Chen, 2002 [25]. In this case, the term on the second line of Eq. (32) reduces to

$$\Omega_{\kappa}^2 [\Delta_3 + 2(\Delta_1 - 1/2) + 3/2] = 2\Omega_{\kappa}^2 \Delta_2.$$

Note that our calculation yields a different  $\Delta_2$  than that given in Ref. [25]:  $\Delta_2^{\text{Zhao}} = 5/2 + \dots$ , whereas here  $\Delta_2 = 7/4 + \dots$  [cf. Eq. (22)]. Our  $\Delta_2$  gives slightly larger growth rates, as will be shown in the benchmark in Fig. 6 below.

### Quasi-neutrality condition

After eliminating  $\partial_t \delta \Psi_e$  with the help of Eq. (30), the quasi-neutrality condition becomes an algebraic equation, which may be written as

$$\begin{aligned}
\left[ \frac{1}{\tau_{ei}^T} + \Gamma_{0i} - (H_\omega - Z_E \tau_{Ei}^n \tau_{iE}^T) \right] \delta U_e &= -i \delta E_e + [2(\Omega_{\kappa i} + \Omega_{pi}) (1 - \Gamma_{0i} \Delta_{1i}) - \Omega_{pi} (1 - \Gamma_{0i})] \delta \Psi_e \\
&\quad + H_{U\Psi} \delta \Psi_e + (1 - \Gamma_{0i} \Delta_{0i}) \delta C_e + H_{UC} \delta C_e \\
&\quad - \frac{1}{\tau_{ei}^T} \langle J_0 \delta G \rangle_i - \frac{\tau_{Ei}^n}{\tau_{ei}^T} \langle J_0 \delta G \rangle_E.
\end{aligned} \tag{34}$$

The energetic particle terms are

$$\begin{aligned}
H_{U\Psi} &= Z_E \tau_{Ei}^n \tau_{iE}^T \langle (1 - J_0^2) \omega_d \Theta F_0 \rangle_E \xrightarrow{F_M} \tau_{Ei}^n [2(\Omega_{\kappa i} + \Omega_{pi}) (1 - \Gamma_{0E} \Delta_{1E}) - \Omega_{pi} (1 - \Gamma_{0E})], \\
H_{UC} &= \tau_{Ei}^n \left\langle \left( 1 - \frac{2J_1 J_0}{\lambda} \right) \mu B \Theta F_0 \right\rangle_E \xrightarrow{F_M} \tau_{Ei}^n (1 - \Gamma_{0E} \Delta_{0E}).
\end{aligned} \tag{35}$$

The moments of the transformation  $\delta G \rightarrow \delta g$  are:

$$-\frac{\langle J_0(\delta G - \delta g) \rangle_s}{\tau_{ei}^T} = \frac{Z_s \tau_{es}^T}{\tau_{ei}^T} [\langle J_0^2 \Theta F_0 \rangle_s \delta U_e + \langle \omega_d J_0^2 \Theta F_0 \rangle_s \delta \Psi_e] + \frac{1}{\tau_{ei}^T} \left\langle \mu B \frac{2J_1 J_0}{\lambda} \Theta F_0 \right\rangle_s \delta C_e$$

$$\xrightarrow{F_M} Z_s \tau_{is}^T \Gamma_{0s} \delta U_e + \Gamma_{0s} [2\Omega_{\kappa i} \Delta_{1s} + \Omega_{pi} (2\Delta_{1s} - 1)] \delta \Psi_e + \Gamma_{0s} \Delta_{0s} \delta C_e. \quad (36)$$

Given the orderings described in Section 2.1; in particular,  $\tau_{iE}^T \sim \tau_{Ei}^n \sim \mathcal{O}(\delta^2 \dots \delta)$ , we expect the contribution of energetic ions to the quasi-neutrality condition to be small.

### Magnetic compression

After eliminating  $\partial_t \delta \Psi_e$  with the help of Eq. (30), the perpendicular Ampère's law becomes an algebraic equation, which may be written as

$$\left( \hat{B}^2 + \mathcal{T}_i A_\Sigma^2 A_\omega \right) \delta C_e = -i \mathcal{T}_i A_\Sigma \delta E_e + \mathcal{T}_i A_\Sigma A_\omega \delta U_e + \mathcal{T}_i A_\Sigma H_{\Psi\Psi} \delta \Psi_e$$

$$+ \mathcal{T}_i A_\Sigma [2(\Omega_{\kappa i} + \Omega_{pi})(1 - \Gamma_{0i} \Delta_{1i}) - \Omega_{pi}(1 - \Gamma_{0i}) - \omega_{*i}(1 - \Gamma_{0i} \Upsilon_{1i})] \delta \Psi_e$$

$$+ \mathcal{T}_i \omega_{*i} \tau_{ei}^T (1 + \eta_e) \delta \Psi_e + \mathcal{T}_i \omega_{*i} \Gamma_{0i} [\Delta_{0i} + \eta_i (1 - 2b_i \Delta_{0i})] \delta \Psi_e + H_{C\Psi} \delta \Psi_e$$

$$+ \frac{\mathcal{T}_i}{\sqrt{b_i} \tau_{ei}^T} \langle v_\perp J_1 \delta G \rangle_i + \frac{\mathcal{T}_i \tau_{Ei}^n}{\sqrt{b_E} Z_E \tau_{ei}^T \tau_{iE}^T} \langle v_\perp J_1 \delta G \rangle_E; \quad (37)$$

where

$$A_\Sigma = -[(1 - \Gamma_{0i} \Delta_{0i}) + H_{UC}] / A_\omega.$$

The energetic particle term  $H_{C\Psi}$  is

$$H_{C\Psi} = -\mathcal{T}_i \tau_{Ei}^n \left\langle \frac{2J_1 J_0}{\lambda} \mu B \omega_*^T F_0 \right\rangle_E \xrightarrow{F_M} \mathcal{T}_i \tau_{Ei}^n \omega_{*E} \Gamma_{0E} [\Delta_{0E} + \eta_E (1 - 2b_E \Delta_{0E})]. \quad (38)$$

The moments of the transformation  $\delta G \rightarrow \delta g$  are:

$$\mathcal{T}_i \frac{\langle v_\perp J_1 (\delta G - \delta g) \rangle_s}{Z_s \tau_{ei}^T \tau_{is}^T \sqrt{b_s}} = -\frac{\mathcal{T}_i}{\sqrt{b_s}} [\langle v_\perp J_0 J_1 \Theta F_0 \rangle_s \delta U_e + \langle \omega_d v_\perp J_0 J_1 \Theta F_0 \rangle_s \delta \Psi_e]$$

$$- \frac{\mathcal{T}_i}{\sqrt{b_s}} \frac{\tau_{si}^T}{Z_s} \left\langle v_\perp \mu B \frac{2J_1^2}{\lambda} \Theta F_0 \right\rangle_s \delta C_e$$

$$\xrightarrow{F_M} -\frac{\mathcal{T}_i \tau_{si}^T}{Z_s} \Gamma_{0s} [\Omega_{\kappa i} (1 + 2\Delta_{0s} - 2b_s \Delta_{0s}) + \Omega_{pi} (1 + \Delta_{0s} - 2b_s \Delta_{0s})] \delta \Psi_e$$

$$- \frac{2\mathcal{T}_i \tau_{si}^T}{Z_s} \Gamma_{0s} \Delta_{0s} \delta C_e - \mathcal{T}_i \Gamma_{0s} \Delta_{0s} \delta U_e. \quad (39)$$

The final form used in AWECs is obtained by substituting Eq. (37) into Eq. (34) to eliminate  $\delta C_e$ .

## 3 Numerical methods

Equations (25), (29), (30), (34) and (37) are solved as an initial value problem with the particle-in-cell (PIC) code AWECs using a Runge-Kutta scheme. A finite number of markers is employed to sample the phase space. A modified  $\delta f$  method appropriate for particle-conserving compressible dynamics is adopted, with marker weights chosen such as to allow a uniform distribution in energy. In this section, these methods are described in detail and an outline of the computational cycle is given. In the following, grid points and markers are labeled by the indices  $i \in [1, N_g]$  and  $j \in [1, N_m]$ , respectively. A ‘‘cell’’ is the space between two grid points and its size is  $\Delta\theta = \theta_{i+1} - \theta_i$ .

### 3.1 PIC method

While marker positions  $\theta_j$  vary continuously, fields are sampled at discrete grid points  $\theta_i$ . In order to solve the field equation, the contribution of each marker to the particle density at each grid point must be determined. Conversely, the marker motion is subject to electromagnetic forces known only on the

discrete grid. The PIC method employed here is a 1st-order scheme that provides smooth mapping between markers and the grid. In this method, each marker  $j$  is replaced by a top-hat function  $\Pi$  of width  $\Delta\theta$  centered at  $\theta_j$ , where the definition of the top-hat function is  $\Pi(x) = 1$  for  $|x| < 1$ , and zero elsewhere. The sum of these finite-sized markers integrated over the interval  $\theta \in [\theta_i - \Delta\theta/2, \theta_i + \Delta\theta/2]$  and divided by  $\Delta\theta$  yields the number of markers  $N_i$  contributing to grid point  $\theta_i$ :

$$\frac{1}{\Delta\theta} \sum_{j=1}^{N_m} \int_{\theta_i - \Delta\theta/2}^{\theta_i + \Delta\theta/2} d\theta \Pi\left(\frac{\theta - \theta_j}{\Delta\theta/2}\right) = \sum_j S(\theta_i - \theta_j) \equiv N_i. \quad (40)$$

This local integration gives rise to the triangular shape function<sup>5</sup>

$$S(\theta - \theta_j) = \begin{cases} 1 - 2|\theta - \theta_j|/\Delta\theta & : |\theta - \theta_j| \leq \Delta\theta/2, \\ 0 & : \text{elsewhere.} \end{cases} \quad (41)$$

Note that  $\int d\theta S = \Delta\theta$ . At the boundary points of the domain in which markers are loaded, the marker weights are doubled. This effectively simulates the effect of a plasma beyond these points, which is a mirror image of the plasma inside.

## 3.2 Modified $\delta f$ method for compressible dynamics

### Description of the method

Equation (15) may be compactly written as

$$\mathcal{L}_0 \delta G_s + i\omega_{ds} \delta G_s = -\delta \mathcal{L} f_{0s},$$

where  $\mathcal{L}_0 = \partial_t + v_{\parallel} \partial_l$  is the inverse propagator along a field line. The  $\omega_{ds}$  term can be eliminated by a transformation from the guiding centers to magnetic drift centers [4]

$$\begin{aligned} \delta G_s &= \delta G_{ds} e^{-i\delta_{ds}} \quad \text{with} \quad \delta_{ds} = \int_{-\infty}^t d\tau \omega_{ds}(\tau) \\ &\Rightarrow \mathcal{L}_0 \delta G_{ds} = -\delta \mathcal{L} f_{0s} e^{i\delta_{ds}}. \end{aligned} \quad (42)$$

The integrating factor  $\exp(-i\delta_{ds})$  was expected to help avoid numerical problems associated with the secular term in  $\omega_{ds}$  ( $\omega_{ds} \propto \theta$  for  $|\theta| \gg 1$ ). To date, however, no significant difference was found between AWECS runs solving Eq. (15) and those solving Eq. (42).

For an isotropic Maxwellian equilibrium distribution,  $f_0 = n_0(r) F_M(r, \mathcal{E})$ , the particle density at high energies  $\mathcal{E}$  is low, so a corresponding marker distribution would introduce a large amount of discretization noise through the highest-order velocity moment, which in our case is  $\langle \omega_d J_0 \delta G \rangle$ . One way to avoid this problem is to load the markers with a probability distribution function (PDF)  $P_{\hat{\sigma}}$ , defined by  $P_{\hat{\sigma}} W_0 = f_0$ , and require that  $\partial_{\mathcal{E}} P_{\hat{\sigma}} = 0$ . For the perturbed particle distribution this means that  $P_{\hat{\sigma}} \delta W = \delta f$ , or, equivalently,  $\delta W/W_0 = \delta f/f_0$ , where  $W_0$  and  $\delta W$  are equilibrium and perturbed weight functions.

In the conventional  $\delta f$  method, the PDF  $P_{\hat{\sigma}}$  for the markers is chosen to be such that  $\mathcal{L}_0 P_{\hat{\sigma}} = 0$ , and one solves the equation for the weight function  $\delta W$  instead of  $\delta f$ . In the present case, that equation would read

$$[\mathcal{L}_0 - (\partial_l v_{\parallel})] \delta W = -W_0 \delta \mathcal{L} (\ln f_{0s}).$$

In AWECS, we adopt the alternative scheme utilized previously in Ref. [14], where  $P_{\hat{\sigma}}$  is required to satisfy the continuity equation for compressible dynamics,

$$\partial_t P_{\hat{\sigma}} + \partial_{\theta} (v_{\parallel} P_{\hat{\sigma}}) = 0. \quad (43)$$

---

<sup>5</sup>It may be more intuitive to refer to  $\Pi$  as the ‘‘shape’’ of a particle. The function  $S$  describes the mapping between marker position and the finite-difference grid and is sometimes called ‘‘assignment function.’’ In practice, we only deal with  $S$  and it has become customary to simply call it ‘‘shape function.’’

Defined this way, the spatial marker distribution represents closely the physical particle distribution along a field line. Therefore, we can solve the GKE for the physical particle distribution function,

$$\mathcal{L}_0 \delta G_{ds} = -\delta \mathcal{L} f_{0s} \exp(i\delta_{ds}),$$

along unperturbed marker orbits. The difference between markers and physical particles manifests itself only in the discretized velocity space integrals, where an additional weight factor appears (see Section 3.2).

### Marker loading

It is convenient to introduce the pitch angle variable  $A$  defined as

$$A = \frac{\mu B_0}{\mathcal{E}} = \frac{v_\perp^2 B_0}{v^2 B} = \frac{\sin^2(\varphi)}{\hat{B}}; \quad (44)$$

where  $\varphi = \varphi(B)$  is the pitch angle; i.e., the angle between the local magnetic field  $\mathbf{B}$  and the velocity vector  $\mathbf{v}$ . Note that for particles which are trapped in a magnetic mirror, the pitch angle coordinate  $A$  is related to the turning points  $\pm\theta_b$  (“bounce angles”) through  $A = 1/\hat{B}(\theta_b)$  which follows from  $v_\perp^2(\theta_b) = 2\mathcal{E}$ . For the purpose of marker loading, we take  $A$  to be an independent velocity space coordinate instead of the magnetic moment  $\mu$ . Recall that

$$\mathcal{E} = v^2/2 = (v_\perp^2 + v_\parallel^2)/2, \quad \mu = v_\perp^2/(2B),$$

so the velocity space coordinates do not contain the particle mass. For the parallel velocity  $v_\parallel$  of a marker with  $(A, \mathcal{E})$  at a given location  $\theta_j$ , parametrized by  $B = B(\theta_j)$ , we obtain the following expression:

$$|v_\parallel| = \sqrt{v^2 - v_\perp^2} = \sqrt{2\mathcal{E}} \sqrt{1 - A\hat{B}} = \sqrt{2\mathcal{E}} u, \quad \text{with } u = \sqrt{1 - A\hat{B}}. \quad (45)$$

Note that the normalized parallel velocity  $u$  satisfies  $\partial_\mathcal{E} u = 0$ .

In order for the plasma conditions to remain constant in time, the markers must be loaded in equilibrium:  $\partial_t P_\sigma = 0$ . Thus, Eq. (43) implies  $\partial_t(v_\parallel P_\sigma) = 0$ ; that is,

$$v_\parallel P_\sigma = C(A, \mathcal{E}).$$

Since  $\partial_\mathcal{E} A = 0$ , a simple PDF which satisfies the condition  $v_\parallel P_\sigma = C(A, \mathcal{E})$  and allows to initialize uniformly in energy ( $\partial_\mathcal{E} P_\sigma = 0$ ) is obtained with the choice  $C(A, \mathcal{E}) = C_0 \sqrt{2\mathcal{E}}$ :

$$P_\sigma(A, B) = \frac{C_0 \sqrt{2\mathcal{E}}}{|v_\parallel|} = \frac{C_0}{\sqrt{1 - A\hat{B}}} = \frac{C_0}{u}. \quad (46)$$

The size of the computational domain,  $\theta \in [-\theta_{\max}, \theta_{\max}]$  must be sufficiently large to avoid unphysical reflections at the boundaries. However, markers are only required in the region where the unstable modes have a significant amplitude. In AWECS, the parameter  $N_p$  determines the number of loading periods, and the size of this domain,  $2\pi N_p$ , can usually be chosen smaller than the computational domain,  $2\theta_{\max}$  (see the convergence study in Section 7). In the region without markers, we set  $\delta G = 0$ .

The markers are loaded according to the following procedure:

1. Spatial loading. Integrating the marker PDF  $P_\sigma$  given by Eq. (46), and using  $\sum_\sigma P_\sigma = 2P_\sigma$ , we obtain

$$\sum_\sigma \int_{\mathcal{E}_{\min}}^{\mathcal{E}_{\max}} d\mathcal{E} \int_{A_{\min}}^{A_{\max}} dA \int_{\theta_1}^{\theta_2} d\theta P_\sigma = 2C_0(\mathcal{E}_{\max} - \mathcal{E}_{\min}) \int_{\theta_1}^{\theta_2} d\theta \left[ -\frac{2}{\hat{B}} \sqrt{1 - A\hat{B}} \right]_{A_{\min}}^{A_{\max}}; \quad (47)$$

which is valid for any interval  $[\theta_1, \theta_2]$ . Hence, the marker density  $n(\theta)$  is given by

$$n(\theta) \propto w(\theta) = \frac{1}{\hat{B}} \left( \sqrt{1 - A_{\min}\hat{B}} - \sqrt{\max\{1 - A_{\max}\hat{B}, 0\}} \right) = \frac{u_{\max} - u_{\min}}{\hat{B}}. \quad (48)$$

The weight function  $w(\theta)$  is then used to map a uniform distribution of random numbers  $R_j \in [0, 1]$  to a nonuniform distribution in  $\theta$ :

(i) Numerical integration of  $w$  gives the cumulative distribution

$$\overline{W}(\theta) = \int_{\theta_1}^{\theta} d\theta' w(\theta').$$

(ii) From this, we sample uniformly distributed random values,

$$R_j \overline{W}(\theta_2) = \overline{W}_j \in [0, \overline{W}(\theta_2)].$$

In ballooning space, the integral limits are  $\theta_1 = 0$  and  $\theta_2 = \max\{\theta_b\} - \varepsilon_{\text{num}}$  for trapped particles, while for passing particles  $\theta_2 = \pi - \varepsilon_{\text{num}}$ . Here,  $\varepsilon_{\text{num}}$  is the smallest number that can be represented numerically in double precision.

(iii) The map  $\overline{W}^{-1}(\theta) : \overline{W}_j \rightarrow \theta_j$  then yields non-uniformly distributed marker positions  $\theta_j$ . Since  $\overline{W}$  is known only at discrete grid points, the inversion  $\overline{W}^{-1}$  is done using linear interpolation.

(iv) Offsets  $n_{pj}\pi$ , with  $n_{pj} = 1, \dots, (N_p - 1)$ , are added to spread markers over all periods.

2. Pitch angle distribution: The largest allowed value for  $A$  depends on the location  $\theta$  (parametrized by  $B$ ). The constraint to be obeyed is most easily written for the parallel velocity, which must satisfy

$$v^2 - v_{\perp}^2 = v_{\parallel}^2 \geq 0.$$

Thus, we first determine the limits of  $u \equiv |v_{\parallel}|/\sqrt{2\mathcal{E}}$  for a chosen interval  $[A_{\min}, A_{\max}]$ , using the relation

$$u = \sqrt{1 - A\hat{B}}.$$

These are

$$u_{\max} = \sqrt{1 - A_{\min}\hat{B}}, \quad u_{\min} = \sqrt{\max\{1 - A_{\max}\hat{B}, 0\}}.$$

Next, we sample random values  $u_j$ , uniformly distributed over the interval  $[u_{\min}, u_{\max}]$ , and calculate the pitch angle variable  $A_j = (1 - u_j^2)/\hat{B}$ . Note that passing particles satisfy  $A_{\max} = A_{\pi}$ , where  $A_{\pi} \equiv 1/\hat{B}(\pi) = 1 - \varepsilon$ .

3. Energy distribution: We distribute marker energies uniformly in a chosen interval  $[\mathcal{E}_{\min}, \mathcal{E}_{\max}]$ . The appropriate limits depend on the problem at hand; in particular, the order of the highest energy moment. In AWECS, the energy coordinate  $\mathcal{E}_j$  is also used to store the sign of the parallel velocity,  $\hat{\sigma} = \text{sign}(v_{\parallel})$ .

After loading  $N_{ms}/4$  markers onto the positive  $\theta$  and  $\mathcal{E}$  axes as described above, the distribution is copied to the respective negative axis. The number of markers used for species  $s$  is thus given by  $N_{ms} = N_{fs} \times 4 \times N_p$ , with input parameters  $N_{fs}$  and  $N_p$ . The remaining input parameters specifying the marker distribution are

$$v_{\min}, \quad v_{\max}, \quad \underbrace{0 < a_{\pi\min} < a_{\pi\max} < 1}_{\text{passing}}, \quad \underbrace{0 < \theta_{b,\min} < \theta_{b,\max} < \pi}_{\text{trapped}}, \quad (49)$$

such that

$$\mathcal{E} \in \frac{1}{2} \times [v_{\min}^2, v_{\max}^2], \quad A_{\text{pass}} \in A_{\pi} \times [a_{\pi\min}, a_{\pi\max}], \quad A_{\text{trap}} \in [1/\hat{B}(\theta_{b,\max}), 1/\hat{B}(\theta_{b,\min})].$$

The fraction of trapped particles can only be manipulated through the inverse aspect ratio  $\varepsilon$ . However, the number of markers used to sample the phase spaces of trapped and passing particles can be varied independently.

The marker loading is completed with the calculation of the normalization constant  $C_0$ . If we equate the integral of  $P_{\hat{\sigma}}$  in Eq. (47) with that of the Klimontovich distribution,

$$P_{\hat{\sigma}} = \sum_{j=1}^{N_m} \delta(\mathcal{E} - \mathcal{E}_j) \delta(A - A_j) \delta(\theta - \theta_j) \delta(\hat{\sigma} - \hat{\sigma}_j), \quad (50)$$

we obtain the following equation for the constant  $C_0$ :

$$C_0 = \frac{N_m(\theta_{\min}, \theta_{\max})}{4(\mathcal{E}_{\max} - \mathcal{E}_{\min})b_1} \quad \text{with} \quad b_1 = \int_{\theta_{\min}}^{\theta_{\max}} d\theta \frac{u_{\max} - u_{\min}}{\hat{B}}; \quad (51)$$

where  $N_m(\theta_{\min}, \theta_{\max})$  is the number of markers in the interval  $\theta \in [\theta_{\min}, \theta_{\max}]$ . In the PIC method, the spatial Dirac deltas  $\delta(\theta - \theta_j)$  in the Klimontovitch distribution (50) are replaced by finite-sized markers  $S(\theta - \theta_j)/\Delta\theta$  [cf. Eq. (40)]. The local normalization constant  $C_{0i}$  at a grid point  $i$  is obtained by carrying out the integral in Eq. (47) over the spatial interval  $\theta \in [\theta_i - \Delta\theta/2, \theta_i + \Delta\theta/2]$  and substituting Eq. (40) for the left-hand side:

$$\sum_{j=1}^{N_m} S(\theta_i - \theta_j) = N_i \approx 4C_{0i}(\mathcal{E}_{\max} - \mathcal{E}_{\min}) \left[ \frac{u_{\max} - u_{\min}}{\hat{B}} \right]_i \Delta\theta; \quad (52)$$

where  $\hat{B}$  was taken to be constant within the small integration interval. As in Eq. (40),  $N_i$  denotes the effective number of markers at the grid point  $i$  and we write

$$C_{0i} = \frac{N_i \hat{B}_i}{4\Delta\theta(\mathcal{E}_{\max} - \mathcal{E}_{\min}) [u_{\max} - u_{\min}]_i}. \quad (53)$$

The normalization constant is then obtained by averaging over all populated grid points:

$$C_0 = \sum_{i=1}^{N_g} C_{0i} / \sum_{i=1}^{N_g} \delta_{N_i > 0}; \quad \text{where} \quad \delta_{N_i > 0} = \begin{cases} 1 & : N_i > 0, \\ 0 & : \text{else.} \end{cases} \quad (54)$$

Alternatively, we could define

$$C_0 \Delta\theta = \left( \sum_i N_i \right) / \left\{ 4(\mathcal{E}_{\max} - \mathcal{E}_{\min}) \sum_i [(u_{\max} - u_{\min})/\hat{B}]_i \right\},$$

which gives a very similar value. However, the method of calculating local values  $C_{0i}$  allows to check whether  $C_{0i}$  is indeed approximately the same everywhere.

### Velocity space average

The velocity space average of a quantity  $X = X(\mathcal{E}, \mu, \theta)$  is given by

$$\langle X \rangle(\theta) = 2\pi \sum_{\hat{\sigma}} \int_0^{\infty} d\mathcal{E} \int_0^{E/B} d\mu \frac{B}{|v_{\parallel}|} X(\mathcal{E}, \mu, \theta). \quad (55)$$

Substituting the pitch angle variable  $A = \mu B_0 / \mathcal{E}$  for  $\mu$ , and the normalized velocity  $u = |v_{\parallel}|/\sqrt{2\mathcal{E}}$  for  $|v_{\parallel}|$ , and sampling the phase space by including the factor  $P_{\delta}/P_{\hat{\sigma}}$  into the integrand yields

$$\begin{aligned} \langle X \rangle(\theta) &\approx 2\pi \sum_{\hat{\sigma}} \int_0^{\infty} d\mathcal{E} \int_0^{1/\hat{B}} dA \frac{\hat{B}\mathcal{E}}{|v_{\parallel}|} \frac{P_{\delta}}{P_{\hat{\sigma}}} X(\mathcal{E}, A, \theta) \\ &= \frac{2\pi}{\sqrt{2}C_0} \sum_{\hat{\sigma}} \int_0^{\infty} d\mathcal{E} \int_0^{1/\hat{B}} dA \hat{B} \sqrt{\mathcal{E}} P_{\delta} X(\mathcal{E}, A, \theta); \end{aligned} \quad (56)$$

where  $P_{\hat{\sigma}} = C_0 \sqrt{2\mathcal{E}}/|v_{\parallel}|$  was used. Replacing the Dirac distribution  $\delta(\theta - \theta_j)$  in Eq. (50) by the shape function  $S(\theta - \theta_j)/\Delta\theta$ , we obtain

$$\langle X \rangle_i \approx \frac{2\pi}{\sqrt{2}C_0 \Delta\theta} \sum_{j=1}^{N_m} \hat{B}(\theta_j) \sqrt{\mathcal{E}_j} S(\theta_i - \theta_j) X(\mathcal{E}_j, A_j, \theta_j). \quad (57)$$

### 3.3 Boundary conditions

The size of the simulation domain,  $2\theta_{\max}$ , depends largely on the magnetic shear  $s$ . The larger  $s$  the faster any wave with finite radial extent is damped with increasing  $|\theta|$ . However, some eigenmodes, such as  $\alpha$ TAEs, couple to the Alfvén continuum, which consists of waves singular in  $r$ . Since  $r$  and  $\theta$  are related through a Fourier transform, continuum waves in  $\theta$ -space take the form of undamped outgoing harmonic waves. In order to prevent unphysical reflections at the boundaries of the finite computational domain, the outgoing-wave boundary condition is facilitated by a “boundary filter” of the form

$$w(\theta) = \begin{cases} 1 & : |\theta| \leq \theta_{\text{bf}}, \\ \exp\left(-\frac{|\theta| - \theta_{\text{bf}}}{\sigma}\right) & : |\theta| > \theta_{\text{bf}}; \end{cases} \quad (58)$$

which provides for artificial damping. Typically,  $\theta_{\text{bf}} = 0.8 \times \theta_{\max}$  is used.

### 3.4 Filtering

We use the FFTW package (version 2.1.5) for optional low-pass filtering in  $k$ -space. If enabled, the default cut-off is one quarter of the Nyquist wavenumber. In principle, this setting may reduce the accumulation of aliasing errors, but it cannot eliminate them. In linear gyrokinetic simulations, the amount of aliasing is mainly determined by the number of phase space markers and the shape function. To date, no significant effect of filtering on AWECS simulation results has been observed, except for smoother mode structures.

### 3.5 Algorithm

The time integration can be carried out using either a 2nd- or a 4th-order Runge-Kutta scheme [15]. The results presented in following sections were obtained with the 4th-order scheme. The computational cycle may be outlined as follows:

1. Solve the GKE  $\mathcal{L}_0 \delta g = -\delta \mathcal{L} f_{0s} \exp(i\delta_{\text{ds}})$  along unperturbed marker orbits.
2. Push markers along unperturbed particle orbits:  $\theta_j(t) = \int dt' v_{\parallel j}(\theta_j(t'))$ .
3. Calculate velocity space moments of the marker distribution.
4. Evolve the electromagnetic fields  $\delta E_e$  and  $\delta \Psi_e$ , given the moments of  $\delta g$ .
5. Solve the algebraic field equations for  $\delta U_e$  and  $\delta C_e$ , given  $\delta E_e$ ,  $\delta \Psi_e$  and the moments of  $\delta g$ .

AWECS automatically parallelizes on clusters using Message Passing Interface (MPI). A two-dimensional Cartesian processor grid is established in order to allow parallelization over markers and cases. Thus, AWECS is capable of parallelizing case scans and producing organized output without the use of separate script files.

## 4 Benchmark 1: Electrostatic instabilities

### 4.1 Preliminaries: ESITG equations

In order to test the correct implementation of the solver algorithms for field and particle dynamics as well as the PIC method, a simple model for linear electrostatic ion-temperature-gradient-driven (ESITG) modes is implemented in AWECS-ESITG. After renormalizing the time as  $\tilde{t} = t\omega_{*i}$ , with  $\omega_{*i} = q\hat{k}_{0i}\mathcal{T}_i^{1/2}/\varepsilon_n$ , and writing

$$\delta\tilde{\phi} = -\tau_{\text{ei}}^T \delta U_e / \omega = e_i \delta\phi / (m_i \mathcal{T}_i), \quad \delta h_i = \delta g_i / \omega,$$

we obtain the electrostatic limit ( $\delta\Psi_e = \delta C_e = \Omega_p = 0$ ) by letting  $\mathcal{T}_i \rightarrow 0$ . Energetic particles are excluded and the resulting model equations are

$$\delta\tilde{\phi} = \frac{\tau_{ei}^T}{1 + \tau_{ei}^T(1 - \Gamma_{0i})} \langle J_{0i} \delta h_i \rangle, \quad (59)$$

$$\frac{d\theta_j}{dt} = \frac{\varepsilon_n}{q\hat{k}_{0i}} \hat{v}_{\parallel}, \quad (60)$$

$$\frac{d\delta h_i}{dt} = -i\tilde{\omega}_{di} \delta h_i + iF_{Mi} \left[ (\tilde{\omega}_{*i}^T - \tilde{\omega}_{di}) J_{0i} \delta\tilde{\phi} + i \frac{\varepsilon_n}{q\hat{k}_{0i}} \hat{v}_{\parallel} \partial_{\theta} (J_{0i} \delta\tilde{\phi}) \right]; \quad (61)$$

where

$$\tilde{\omega}_{*i}^T = 1 + \eta_i (\hat{\mathcal{E}} - 3/2), \quad \tilde{\omega}_{di} = \varepsilon_n g (\hat{v}_{\perp}^2/2 + \hat{v}_{\parallel}^2), \quad \varepsilon_n = \varepsilon_{pi}(1 + \eta_i).$$

Note that, in the electrostatic limit,  $\delta h_i = \delta g_i/\omega$  in Eq. (61) is related to the perturbed distribution  $\delta f_i$  through the relation

$$\delta f_i = -\frac{e_i}{T_i} F_{Mi} (1 - J_{0i}^2) \delta\phi + J_{0i} \delta h_i,$$

so it has a clear physical meaning:  $J_{0i} \delta h_i$  is  $\delta f_i$  minus the density perturbation caused by the ion polarization drift.

## 4.2 Zero inverse aspect ratio

In order to test the correct implementation of passing particle dynamics, parameter scans with respect to  $\eta_i$ ,  $k_{\vartheta} \rho_s = (\tau_{ei}^T)^{1/2} \hat{k}_{0i}$ ,  $\varepsilon_n$  and  $\tau_{ei}^T$  are carried out for cases with  $\varepsilon = 0$ , studied previously by Dong, Horton & Kim, 1992 (DHK92) [16]. DHK92 solve an integro-differential formulation of the model as an eigenvalue problem. The resulting growth rates  $\gamma$  and frequencies  $\omega_r$  are shown in Fig. 1. Zhao, 2001 (Zhao01) [17] repeated DHK92's calculations with a code that solves Eqs. (59)–(61) as an initial value problem using a predictor-corrector scheme. Both calculations gave very similar results, so we have plotted them as a single curve for each case in Fig. 1(a)–(c). A noticeable difference can be seen only in the  $\tau_{ei}^T$  scan shown in Fig. 1(d). The parameters used are

- Physical parameters:  $\varepsilon = \alpha = 0$ . All other parameters are shown in Fig. 1.
- Numerical parameters:  $N_m = 2048 \times 4 \times 3$ ,  $\theta_{\max} = 20$ ,  $N_g = 256$ ,  $\Delta t = 0.2$ . In this and the following sections, we use  $v_{\min} = 0.01$ ,  $v_{\max} = 5.0$ ,  $a_{\pi\min} = 0.0001$ ,  $a_{\pi\max} = 0.9999$  [cf. Eq. (49)], unless otherwise specified.

Note that DHK92 defines the thermal velocity as  $v_{ti}^{\text{Dong}} = \sqrt{2T_i}$ , so we have scaled their input parameters and results by a factor  $1/\sqrt{2}$  where appropriate ( $k_{\vartheta} \rho_s^{\text{Dong}} = \sqrt{2} k_{\vartheta} \rho_s$ ). Furthermore, we have defined the diamagnetic frequency such that  $\omega_{*i} > 0$ .

Figure 1 shows that the results by DHK92 and Zhao01 (squares) are reproduced accurately by AWECES-ESITG (circles). Runs with 2nd- and 4th-order Runge-Kutta schemes gave identical results.

## 4.3 Cyclone base case

In order to test the correct implementation of trapped particle dynamics, we compare AWECES-ESITG results for the Cyclone base case with those produced by two other codes: an electrostatic version of the gyrokinetic fully-implicit initial-value code GS2 [18], and the global gyrokinetic toroidal particle code GT3D [19]. In the reference cases used, both GS2 and GT3D were run in the massless-electron limit. Both GS2 and AWECES employ the  $s$ - $\alpha$  model and the main difference between the codes lies in the numerical scheme; thus, the results should be quantitatively comparable. When comparing with the global code GT3D, we only look for qualitative similarity between the results. The parameters are:

- Physical parameters: The Cyclone base case parameters are  $\varepsilon = 0.18$ ,  $\eta_i = 3.114$ ,  $\varepsilon_n = 0.45$ ,  $s = 0.776\dots 0.796$ ,  $q = 1.4$ ,  $\tau_{ei}^T = 1.0$  [20]. The actual input parameters used in GS2 and GT3D differ slightly and we use their settings for our calculations. The parameters to be varied are  $\hat{k}_{0i}$  and  $\eta_i$ .



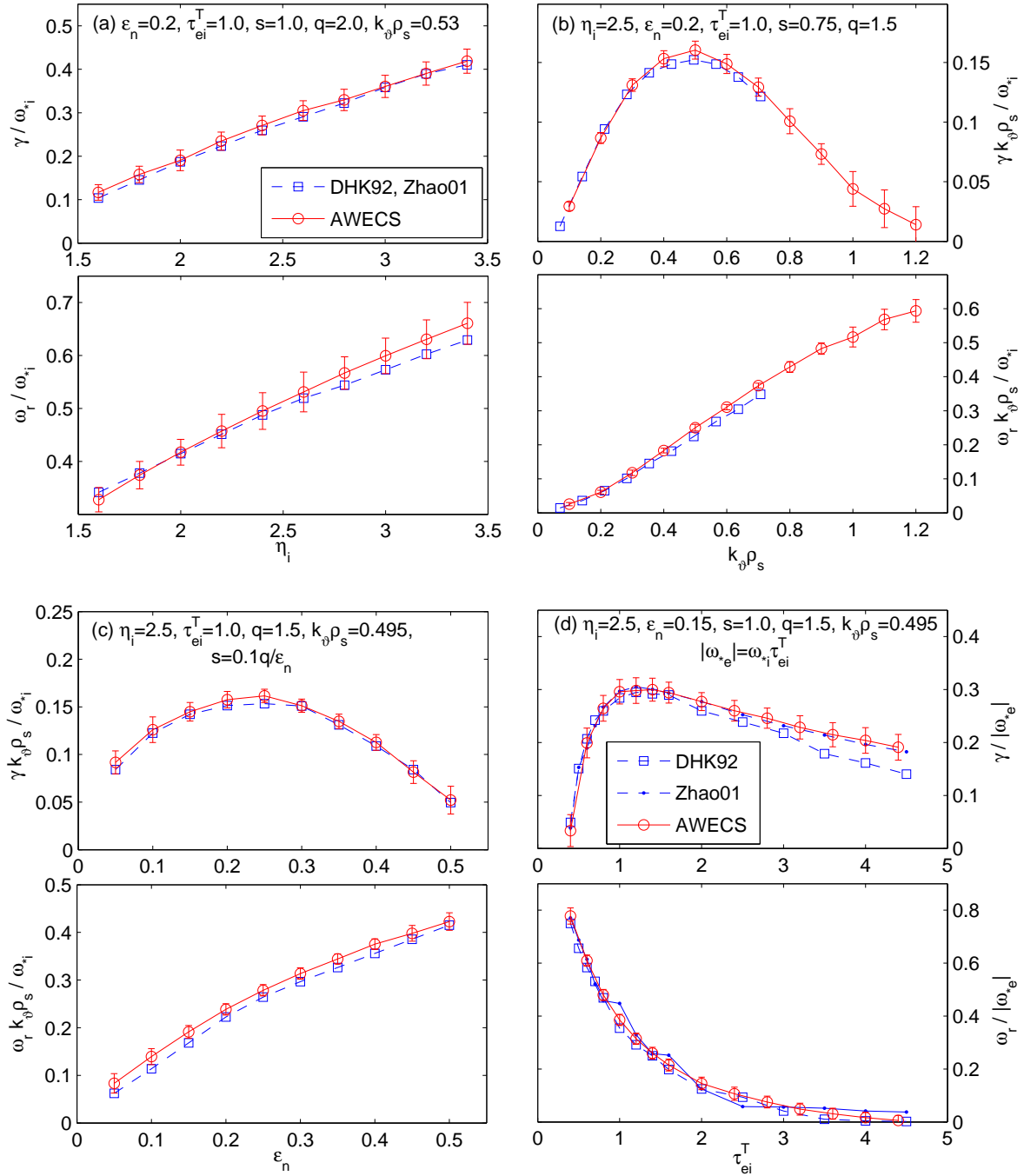


Figure 1: Benchmark of AWECS results for ESITG modes against Refs. [16, 17] (inverse aspect ratio  $\epsilon = 0$ ). Except for the  $\tau_{ei}^T$  scan (d), the results by Dong *et al.*, 1992 (DHK92) [16] and Zhao, 2001 (Zhao01) [17] are very similar and are plotted as a single curve (squares).

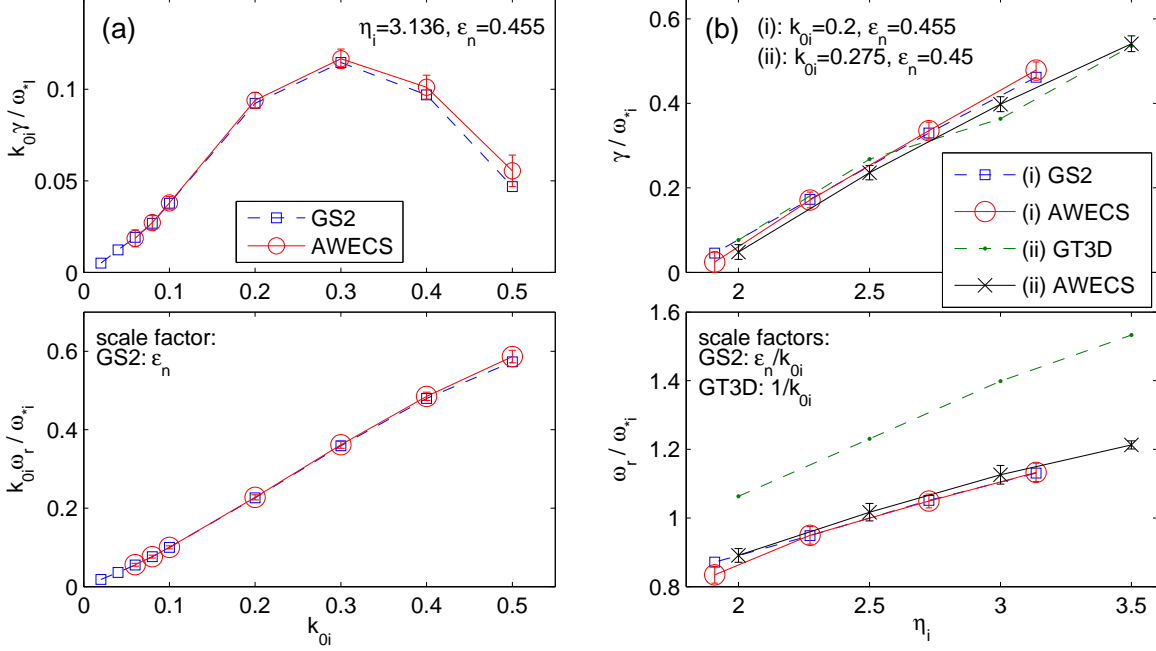


Figure 2: Benchmark of AWECS results for ESITG modes against Cyclone base case calculations performed with GS2 [18] and GT3D [19] (inverse aspect ratio  $\varepsilon = 0.18$ ).

- Numerical parameters:  $N_m = 2048 \times 4 \times 3$ ,  $\theta_{\max} = 20$ ,  $N_g = 256$ ,  $\Delta t = 0.2$ . The bounce angle range is  $\theta_{b,\min} = 0.1^\circ$  and  $\theta_{b,\max} = 179.9^\circ$ .

Figure 2(a) shows ESITG growth rates  $\gamma$  and frequencies  $\omega_r$  in dependence of  $\hat{k}_{0i}$ . The results show good agreement between GS2 and AWECS. Figure 2(b) shows results of an  $\eta_i$  scan. Both growth rates and frequencies agree with GS2 results. The comparison with GT3D shows surprisingly good quantitative agreement in the growth rates  $\gamma$ . The systematic discrepancy of about 20% in the frequencies  $\omega_r$  may be due to the fact that AWECS is a local code and uses the CHT  $s$ - $\alpha$  equilibrium, whereas GT3D is a global code.

## 5 Benchmark 2: Shear-Alfvén instabilities

### 5.1 Preliminaries: MHD SAW equation and terminology

Let us first consider shear Alfvén waves with  $\omega \sim \omega_{A0}$ , ignore the temperature gradient ( $\eta_s = 0$ ), and treat the plasma in the ideal-MHD limit ( $\delta U_e = 0$ ). In the cold-ion limit ( $\omega_r \gg \{k_{\parallel} v_{\parallel}, \omega_{*i}, \omega_{di}\}$ ,  $n_{0E} = 0$  and  $\hat{k}_{0i} \ll 1$ ), the contributions from kinetic terms and  $\delta C_e$  can be neglected and the field equations reduce to the low- $\beta$  ideal-MHD SAW equation

$$\partial_{\theta}(f\partial_{\theta}\delta\Psi_e) + (1 + 2\varepsilon \cos\theta)f\omega^2\delta\Psi_e + \alpha g\delta\Psi_e = 0. \quad (62)$$

FLR effects may be taken into account by retaining the  $\omega_{*pi}$  correction to the inertia term, which yields an MHD SAW equation applicable to a warm plasma [21]. In this case,  $\omega^2$  in Eq. (62) is replaced by  $\omega(\omega - \omega_{*pi})$ . The substitutions  $\delta\Psi_s = \sqrt{f}\delta\Psi_e$  and  $\Omega = \omega - \omega_{*pi}/2$  turn the SAW equation into Schrödinger-like form,

$$\partial_{\theta}^2\delta\Psi_s + (1 + 2\varepsilon \cos\theta)(\Omega^2 - \Omega_*^2)\delta\Psi_s - V_{\text{ball}}\delta\Psi_s = 0; \quad (63)$$

where

$$V_{\text{ball}} = (s - \alpha \cos\theta)^2/f^2 - \alpha \cos\theta/f$$

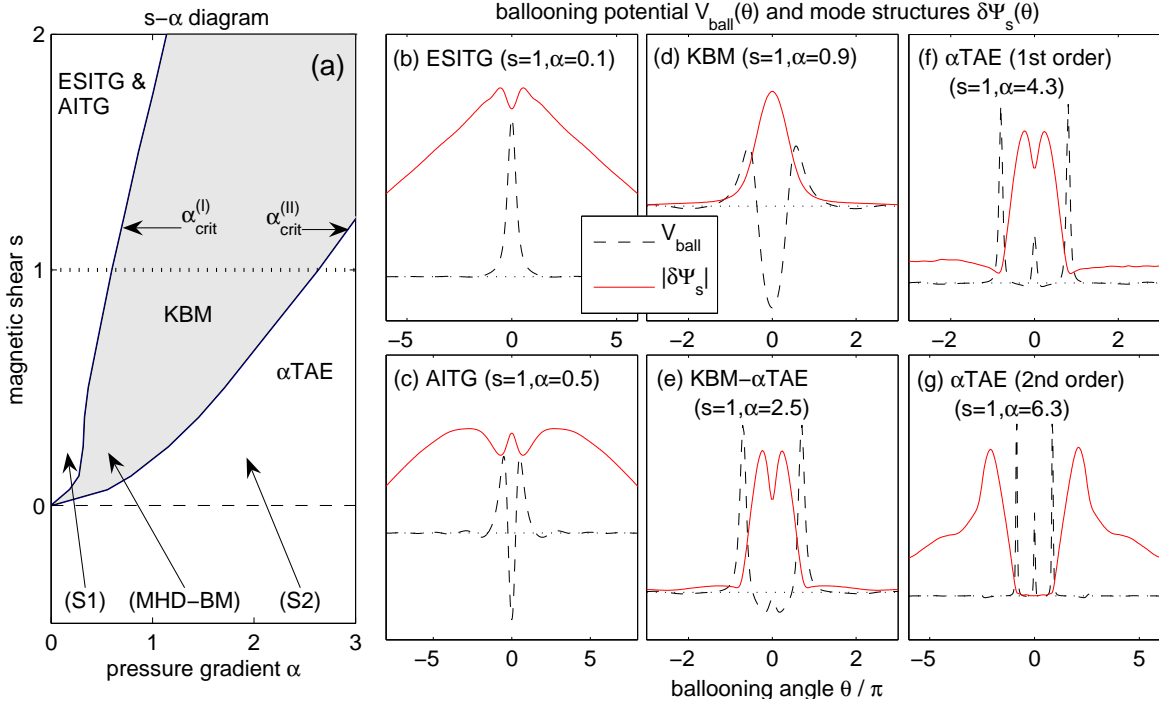


Figure 3: (a):  $s$ - $\alpha$  diagram showing (S1) is the first stable domain, (S2) the second stable domain, and (MHD-BM) the high- $n$  MHD ballooning unstable domain for  $\theta_k = 0$ . (b)–(g): Ballooning potential  $V_{\text{ball}}(\theta|s, \alpha)$  and mode structures of instabilities used for benchmarking. See also Table 1.

$\alpha \ll \alpha_{\text{crit}}^{(I)}$	$\alpha \lesssim \alpha_{\text{crit}}^{(I)}$	$\alpha_{\text{crit}}^{(I)} \lesssim \alpha \lesssim \alpha_{\text{crit}}^{(II)}$	$\alpha \gtrsim \alpha_{\text{crit}}^{(II)}$
ESITG	AITG	KBM	$\alpha$ TAE

Table 1: Instabilities and MHD eigenmodes observed in the benchmark simulations. ESITG: electrostatic ion-temperature-gradient driven mode; AITG: Alfvénic ITG mode; KBM: kinetic ballooning mode;  $\alpha$ TAE:  $\alpha$ -induced toroidal Alfvén eigenmode. See Fig. 3(b)–(g) for corresponding mode structures.

is the ballooning potential and  $\Omega_*^2 = \omega_{*pi}^2/4$  is a constant offset. Equation (63) describes the propagation of periodically driven waves ( $\varepsilon \cos \theta$  factor) in the potential  $V_{\text{ball}}$ . Using an MHD shooting code, we solve Eq. (63) to obtain MHD SAW frequencies in the high- $\beta$  regime, which will be useful to verify results of gyrokinetic simulations.

A derivation similar to that giving Eq. (62), but for marginally stable modes ( $\gamma = 0$ ) with frequencies  $\omega_r = \omega_{*i}$  (again letting  $\eta_i = 0$ ), yields the Connor-Hastie-Taylor (CHT) MHD ballooning equation [12]

$$\partial_\theta^2 \delta\Psi_s - V_{\text{ball}} \delta\Psi_s = 0. \quad (64)$$

Equation (64) determines the stability boundaries of ideal MHD ballooning modes as shown in the  $s$ - $\alpha$  diagram in Fig 3(a). Ballooning modes (BM) are short-wavelength (high- $n$ ) pressure-gradient-driven instabilities similar to the Rayleigh-Taylor interchange instability. They are localized in regions where the field line curvature  $\kappa$  is unfavorable; i.e., where  $\kappa$  has the same sign as the pressure gradient. The  $s$ - $\alpha$  diagram in Fig 3(a) shows the stability boundaries  $\alpha_{\text{crit}}^{(I)}(s)$  and  $\alpha_{\text{crit}}^{(II)}(s)$ , which divide the plane into the first stable domain (S1), the second stable domain (S2), and the MHD ballooning unstable domain (MHD-BM). The diagram shows the case  $\theta_k = 0$ ; the boundaries are modified for finite  $\theta_k$  [22], which is not considered here. The Mercier criterion, which determines the minimum values of  $s$  and  $\alpha$  for interchange instability to occur, is not contained in the CHT  $s$ - $\alpha$  model, so that the (MHD-BM) domain in Fig 3(a) extends to  $s = \alpha = 0$ .

When kinetic particle compression is taken into account, both stable domains (S1) and (S2) become populated with temperature-gradient- and pressure-gradient-driven kinetic instabilities. AWECs has

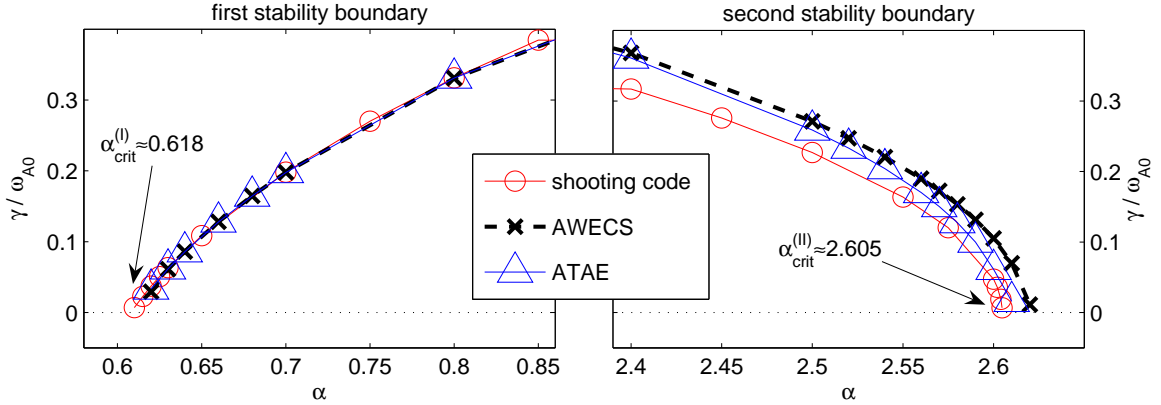


Figure 4: Benchmark of ideal-MHD ballooning stability boundaries. The growth rate  $\gamma$  is plotted as a function of  $\alpha$ , (a) near  $\alpha_{\text{crit}}^{(I)}$  and (b) near  $\alpha_{\text{crit}}^{(II)}$  for  $s = 1.0$ .

	shooting code	ATAE	AWECS
$\alpha_{\text{crit}}^{(I)}$ :	0.608	0.61	0.61
$\alpha_{\text{crit}}^{(II)}$ :	2.605	2.61	2.62

Table 2: Benchmark of MHD ballooning stability boundaries.

been developed to study these modes. In the following, we will consider several previously studied cases to verify that AWECS reproduces earlier results correctly. The instabilities considered are listed in Table 1 and examples for the respective mode structures are shown in Fig. 3(b)–(g).

The instability shown in Fig. 3(g) was discovered by Hirose *et al.* [23]. The mode structure peaks in regions of unfavorable curvature outside the central potential well, so this kind of instability was called “higher-order ballooning mode.” Based on the fact that the frequency  $\omega_r$  approaches a nonzero value as  $\hat{k}_{0i} \rightarrow 0$  (cf. Fig. 15 in Ref. [24]), we conclude that these modes are closely related to discrete MHD Alfvén eigenmodes known to exist in the second MHD ballooning stable domain [7]. These are called  $\alpha$ TAE, so this name is used in the present work. The names “ballooning mode” and “AITG mode” are reserved for instabilities with, in the incompressible thermal ion limit,  $\omega_r(\hat{k}_{0i} \rightarrow 0) \rightarrow 0$  residing inside and outside the (MHD-BM) domain, respectively.

In this section, we benchmark AWECS for shear-Alfvén instabilities in the absence of energetic particles. Benchmarks including energetic particles are presented Section 6.

## 5.2 Ballooning stability boundaries

### Ideal-MHD limit

In Fig. 4 we compare results obtained with a shooting code and two initial value codes, AWECS (4th-order Runge-Kutta) and ATAE (2nd-order leap frog). Both ATAE and the shooting code solve Eq. (62). The size of the computational domain in the initial value codes is  $\theta_{\text{max}} \approx 6\pi \dots 17\pi$ , whereas the shooting code is run with  $\theta_{\text{max}}$  up to  $256\pi$ . Thus, the latter is expected to give the most accurate results for  $\alpha_{\text{crit}}^{(I)}$  or  $\alpha_{\text{crit}}^{(II)}$ , since the mode structure becomes very broad in  $\theta$  when  $\alpha$  approaches marginal stability. The parameters used in AWECS are:  $q = 1.5$ ,  $s = 1.0$ ,  $\varepsilon_n = 0.2$ ,  $\hat{k}_{0i} = 0.001$ ,  $\tau_{ei}^T = 1$ ,  $\eta_s = 0$ . The effects of  $\delta B_{\parallel}$  and  $\Omega_p$  are negligible. Kinetic terms are turned off by setting  $\delta G_i = 0$ .

Results of scans of the parameter  $\alpha$  near the first and second ballooning stability boundary are shown in Fig. 4, and the values obtained for  $\alpha_{\text{crit}}^{(I)}$  and  $\alpha_{\text{crit}}^{(II)}$  are summarized in Table 2. From the good agreement between the three codes it can be concluded that AWECS reproduces the ideal-MHD stability boundaries correctly.

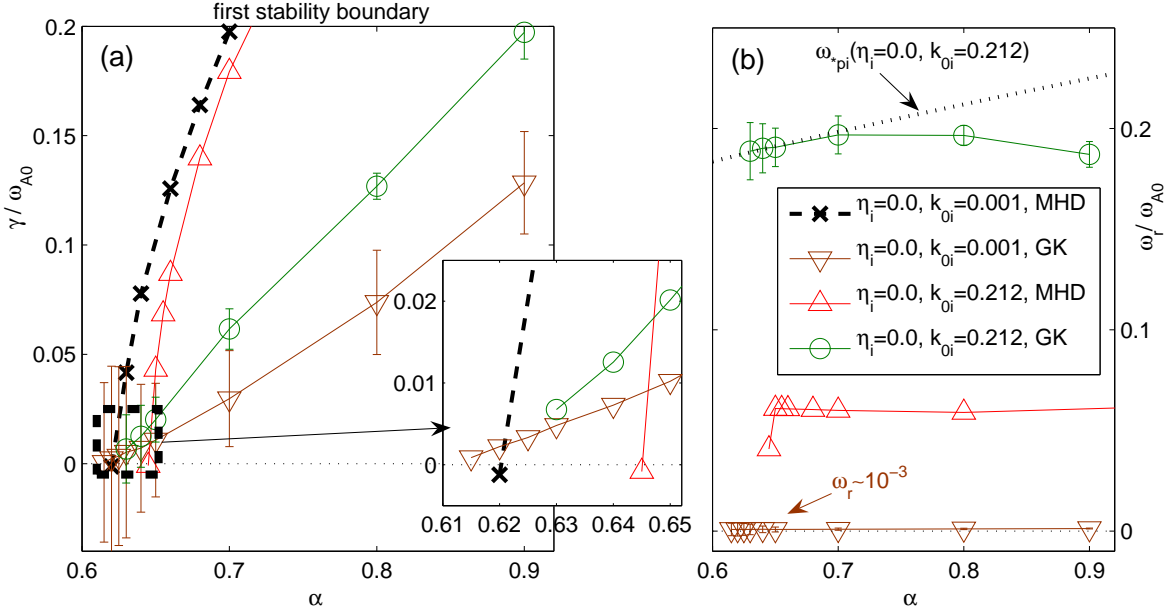


Figure 5: Qualitative behavior of ballooning stability boundaries for finite  $\hat{k}_{0i}$  with kinetic terms turned on (GK) and off (MHD). The growth rate  $\gamma$  (a) and frequency  $\omega_r$  (b) are plotted as a functions of  $\alpha$  near  $\alpha_{\text{crit}}^{(1)}$  for  $s = 1.0$ .

### Finite ion Larmor radius and diamagnetic drift frequency

It can be shown that for  $\eta_i = 0$ , all FLR terms cancel for modes satisfying  $\omega \approx \omega_{*i} = \omega_{*pi}$ , and the CHT ballooning equation (64) is valid for any value of  $\hat{k}_{0i}$  [25]. On the other hand, for the general case  $\omega_r \neq \omega_{*pi}$ , FLR effects were shown to have a stabilizing effect on ballooning modes, yielding somewhat higher values for  $\alpha_{\text{crit}}^{(1)}$  [21].

To verify that AWECS reproduces this qualitative behavior, we repeat the calculation of Section 5.2 with  $\hat{k}_{0i} = 0.001$  and  $\hat{k}_{0i} = 0.212$ , while still setting  $\eta_s = 0$ . Each of these two cases is calculated once with the kinetic terms turned off (“MHD”) and once turned on (“GK”). The results of an  $\alpha$ -scan near the first stability boundary  $\alpha_{\text{crit}}^{(1)}$  are shown in Fig. 5.

In the case (MHD,  $\hat{k}_{0i} = 0.001$ ), the ideal MHD stability boundary is reproduced with good accuracy:  $\alpha_{\text{crit}}^{(1)} \approx 0.615$ . In the case (MHD,  $\hat{k}_{0i} = 0.212$ ), a somewhat larger value  $\alpha_{\text{crit}}^{(1)} \approx 0.64$  is obtained, and the mode has a frequency  $\omega_r \sim \omega_{*i}/3$  near the stability boundary.

Let us now consider the two cases where the kinetic compression terms are retained (“GK”). Extrapolation of the averaged growth rates suggests that the modes become stable near the ideal MHD value  $\alpha_{\text{crit}}^{(1)} \approx 0.615$ . However, the signals are oscillating which gives rise to the large error bars shown in Fig. 5(a) and (b). The oscillation amplitude is larger for  $\hat{k}_{0i} = 0.001$  than for  $\hat{k}_{0i} = 0.212$ .<sup>6</sup> Note that, in contrast to the case (MHD,  $\hat{k}_{0i} = 0.212$ ), the frequency in case (GK,  $\hat{k}_{0i} = 0.212$ ) approaches  $\omega_{*pi}$  near the stability boundary. However, this should be considered coincidental; the two frequencies happen to be the same for this particular value of the wavenumber,  $\hat{k}_{0i} = 0.212$ , while they differ for different values of  $\hat{k}_{0i}$ . Yet, for this particular case, the extrapolated  $\alpha_{\text{crit}}^{(1)}$  coincides with the MHD value, so the result is consistent with the requirement that  $\alpha_{\text{crit}}^{(1)}$  be independent of  $\hat{k}_{0i}$  if  $\omega \sim \omega_{*i} = \omega_{*pi}(\eta_i = 0)$ .

It can be concluded that AWECS correctly reproduces the qualitative behavior of the first ballooning stability boundary for finite values of the ion Larmor radius.

<sup>6</sup>In Section 5.3, we will show that the growth rates in the latter case, (GK,  $\hat{k}_{0i} = 0.212$ ), compare well with the results obtained by Zhao & Chen [25].

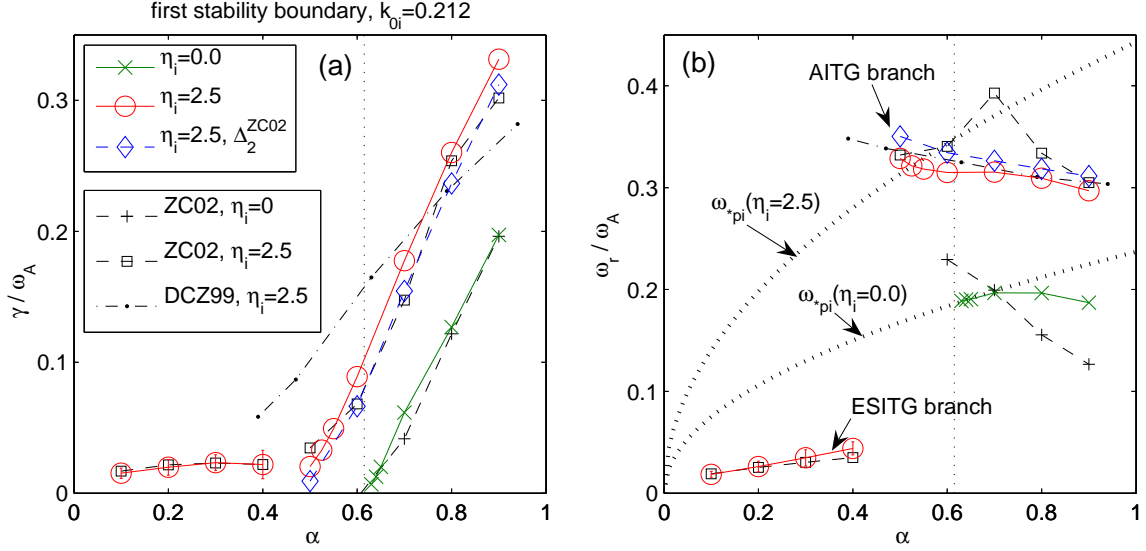


Figure 6: Benchmark in the first ballooning stable domain and near  $\alpha_{\text{crit}}^{(I)}$ . Growth rates (a) and frequencies (b) obtained using AWECs are compared with results obtained by Dong *et al.*, 1999 (DCZ99) [26] and Zhao & Chen, 2002 (ZC02) [25]. Two cases are shown:  $\eta_i = 0$  and  $\eta_i = 2.5$ .

### 5.3 Low- $\beta$ instabilities

The kinetic excitation of electrostatic and Alfvénic instabilities in the first ballooning stable domain and near  $\alpha_{\text{crit}}^{(I)}$  has been studied by Dong, Chen & Zonca, 1999 (DCZ99) using an eigenvalue solver [26], and by Zhao & Chen, 2002 (ZC02) using an initial value code [25]. In this section, we compare AWECs results with data obtained in these two earlier studies. The parameters used are

- Physical parameters:  $q = 1.5$ ,  $s = 1.0$ ,  $\varepsilon_n = 0.2$ ,  $\hat{k}_{0i} = 0.212$  ( $k_{\vartheta}\rho_s^{\text{Dong}} = \sqrt{2}\hat{k}_{0i} = 0.3$ ),  $\tau_{ei}^T = 1.0$ ,  $\eta_i = \eta_e$ ,  $\varepsilon = 0$ .
- Numerical parameters:  $N_m = 512 \times 4 \times 5$ ,  $\theta_{\text{max}} = 40$ ,  $N_g = 512$ ,  $\Delta t = 0.02$ .

AWECs was run with and without magnetic compression and identical results were obtained, which justifies the approximation  $\delta B_{\parallel} = \Omega_p = 0$  used in Refs. [26, 25].

The results are shown in Fig. 6. The growth rates in both cases,  $\eta_i = 0$  and  $\eta_i = 2.5$ , agree well with ZC02’s results<sup>7</sup> and give the same critical  $\alpha$  values:  $\alpha_{\text{crit}}^{(I)}(\eta_i = 0) \approx 0.61$  (KBM) and  $\alpha_{\text{crit}}^{(I)}(\eta_i = 2.5) \approx 0.5$  (AITG). The small discrepancy in the growth rates of the AITG branch is due to the fact that our calculation yields a different coefficient  $\Delta_2$  than that used by ZC02 [see Footnote before Eq. (32)]. If  $\Delta_2^{\text{ZC02}}$  is adopted, AWECs reproduces their result exactly as can be seen in Fig. 6. The AITG frequencies obtained by ZC02 agree with AWECs results, except for one point:  $\alpha = 0.75$ . The reason for this deviation is not known. As mentioned in the previous section, the fact that the frequency  $\omega_r$  approaches  $\omega_{*pi}$  near the stability boundary is coincidental and depends on the value of  $\hat{k}_{0i}$ .

The AITG growth rates by DCZ99 differ from AWECs results and those obtained by ZC02. On the other hand, the frequencies agree well with those obtained using AWECs. The reason for the discrepancy in the growth rates is not known. ZC02 speculated that the problem may be due to the stronger sensitivity of the eigenvalue code to boundary effects. However, the mode structure is broad only near the stability boundary, while the discrepancy persists for  $\alpha > \alpha_{\text{crit}}^{(I)}$  (see also Section 5.4). Moreover, Dong *et al.*, 2004 (DCZJ04) [27] revisited this calculation with  $\theta_{\text{max}} \approx 23$  and reproduced

<sup>7</sup>The growth rates in Ref. [25] seem to be incorrect; a factor of  $\sqrt{2}$  had to be applied in order to obtain agreement with AWECs results. The authors of Ref. [25] have scaled the results by Dong *et al.* [26] by  $\sqrt{2}$  for comparability and may have accidentally scaled their own growth rate data as well. It is not clear whether the frequencies are also affected; in Fig. 6, the frequency values from Ref. [25] are plotted without additional scaling, because the frequencies of the ESITG branch coincide as they are.

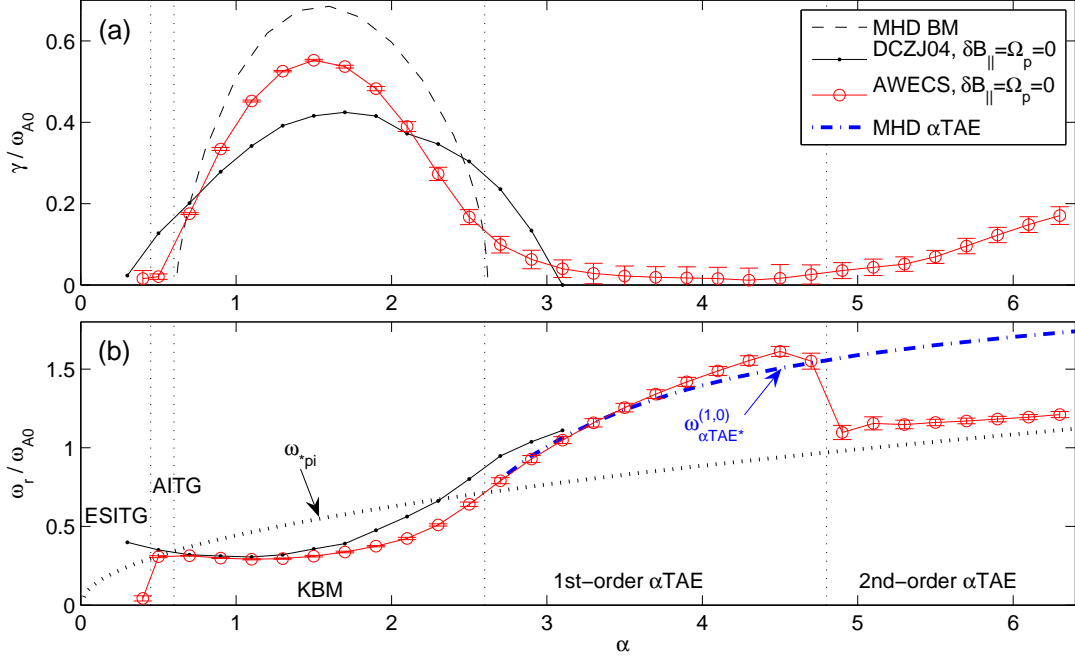


Figure 7: Benchmark for  $s = 1.0$  over a wide range of  $\alpha$  values, including the second ballooning stable domain. Growth rates  $\gamma$  (a) and frequencies  $\omega_r$  (b) obtained using AWECs (solid line with circles) are compared with results obtained by Dong *et al.*, 2004 (DCZJ04) [27] (solid line with dots). In addition, the MHD frequencies for 1st-order  $\alpha$ TAE modes (with  $\omega_{*pi}$  corrections) are plotted (dash-dotted line).

the earlier results by DCZ99, where  $\theta_{\max} \approx 16$  was used. On the other hand, our convergence study in Section 7 will show that  $\theta_{\max} \gtrsim 40$  may be necessary.

Note that the ESITG branch ( $\eta_i = 2.5$ ,  $\alpha < 0.5$ ) is reproduced accurately; both the frequencies and the growth rates agree well. ESITG results are not affected by the different  $\Delta_2$  used by ZC02.

Based on the agreement with results by ZC02 (major discrepancies were explained), we will assume that AWECs correctly computes the properties of finite- $\beta$  ESITG (drift-Alfvén waves), AITG modes and KBMs near the first stability boundary. Discrepancies between the initial value code results and those obtained with the eigenvalue approach used by DCZ99 and DCZJ04 remain to be understood.

## 5.4 High- $\beta$ instabilities

The kinetic excitation of Alfvénic instabilities near  $\alpha_{\text{crit}}^{(\text{II})}$  and in the second ballooning stable domain has been studied by Dong *et al.*, 2004 (DCZJ04) using an eigenvalue solver [27], and by Hirose, Zhang & Elia, 1994 (HZE94) using a shooting code [23]. In this section, we compare AWECs results with results obtained in these two earlier studies.

We begin with a discussion of a case studied by DCZJ04, shown in Fig. 7, where the following parameters were used

- Physical parameters:  $q = 1.5$ ,  $s = 1.0$ ,  $\varepsilon_n = 0.2$ ,  $\hat{k}_{0i} = 0.212$  ( $k_{\vartheta} \rho_s^{\text{Dong}} = \sqrt{2} \hat{k}_{0i} = 0.3$ ),  $\tau_{ei}^T = 1.0$ ,  $\eta_s = 2.5$ ,  $\varepsilon = 0$ .
- Numerical parameters:  $N_m = 512 \times 4 \times 7$ ,  $\theta_{\max} = 40$ ,  $N_g = 512$ ,  $\Delta t = 0.01$ .

In the domain scanned by DCZJ04,  $0.3 \leq \alpha \leq 3.1$ , there is a significant difference in the growth rate and critical  $\alpha$  values. In fact, DCZJ04 reported that no instability was observed for  $\alpha > 3.1$ ; which does not agree with our findings. Although, we are not able to verify the growth rates (except for a convergence study), we can confirm that the instability observed in our results is a physical mode: The frequency in the region  $2.8 \lesssim \alpha \lesssim 4$  follows closely the frequency of the first-order  $\alpha$ TAE obtained with the MHD shooting code, which is denoted by  $\omega_{\alpha \text{TAE}^*}^{(1,0)}$  in Fig. 7 (dash-dotted line). The corresponding mode structure is plotted in Fig. 3(f).

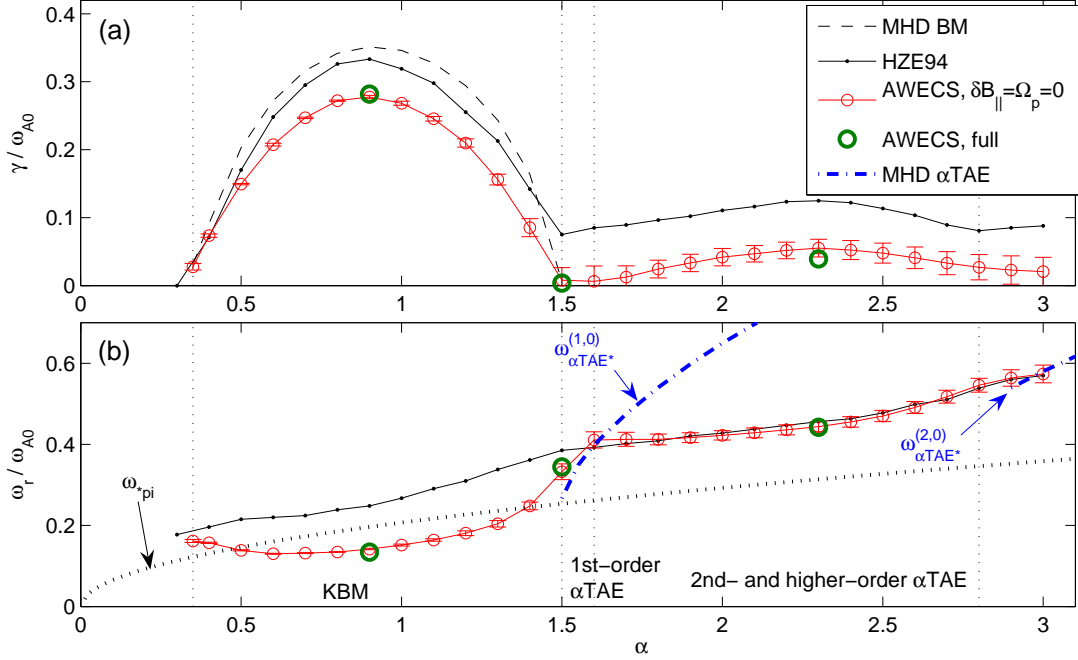


Figure 8: Benchmark for  $s = 0.4$  over a wide range of  $\alpha$  values, including the second MHD ballooning stable domain. Growth rates  $\gamma$  (a) and frequencies  $\omega_r$  (b) obtained using AWECS are compared with results obtained by Hirose *et al.*, 1994 (HZE94) [23]. In (b), the frequencies of the primary unstable mode from HZE94 is plotted. In addition, the MHD frequencies for 1st- and 2nd-order  $\alpha$ TAE modes (with  $\omega_{*pi}$  corrections) are plotted (dash-dotted lines).

Here and in the following,  $\omega_{\alpha TAE*}^{(j,p)}$  denotes the  $\omega_{*pi}$ -corrected MHD frequency of an  $\alpha$ TAE. The “order”  $j \geq 1$  identifies in which potential well the mode amplitude has its maximum, and  $p \geq 0$  counts the number of zeros the mode structure has in potential well  $j$  [7, 28]. The ground state corresponds to  $p = 0$ . The frequencies  $\omega_{\alpha TAE*}^{(j,p)}$  are calculated by a MHD shooting code solving Eq. (63). In this work, only solutions obtained by shooting along the real  $\theta$  axis are considered. A more complete study would require shooting into the complex plane and the application of phase-integral methods [28], since  $\alpha$ TAEs are generally coupled to the Alfvén continuum, either directly or via barrier tunneling. This implies that the problem requires an outgoing-wave boundary condition and that, in general, the solutions of interest are not square integrable. This may explain why the eigenvalue solver DCZJ04 yields a different result.

For  $\alpha > 4.8$ , a 2nd-order  $\alpha$ TAE, with frequency  $\omega_r < \omega_{\alpha TAE*}^{(1,0)}$ , becomes the dominant instability. The corresponding mode structure is plotted in Fig. 3(g). In the MHD limit, this mode is strongly damped in the entire  $\alpha$ -range scanned, so no shooting result for  $\omega_{\alpha TAE*}^{(2,0)}$  is available. However, a  $\hat{k}_{0i}$ -scan at  $\alpha = 6.0$  revealed that  $\omega_r(\hat{k}_{0i} \rightarrow 0)$  is nonzero, which supports our assertion that the mode is an  $\alpha$ TAE.

Let us now proceed to the case studied by HZE94, shown in Fig. 8, where the following parameters were used

- Physical parameters:  $q = 1.2$ ,  $s = 0.4$ ,  $\varepsilon_n = 0.175$ ,  $\hat{k}_{0i} = 0.1$ ,  $\tau_{ei}^T = 1.0$ ,  $\eta_i = \eta_e = 2.0$ ,  $\varepsilon = 0$ .
- Numerical parameters:  $N_m = 512 \times 4 \times 7$ ,  $\theta_{max} = 60$ ,  $N_g = 1024$ ,  $\Delta t = 0.02$ .

It must be noted that the term  $v_{\parallel} \partial_{\theta}$  is omitted in the model used by HZE94, so that important physical effects associated with the transit resonance are missing.

Figure 8(a) shows that the qualitative behavior of the growth rate seen by HZE94 is reproduced by AWECS, both for KBM and  $\alpha$ TAE. The fact that the growth rate in HZE94 are systematically larger is most likely related to their neglect of the transit resonance (Landau damping). Note that the transition to a 3rd-order mode around  $\alpha \approx 2.8$  apparent in HZE94’s results is not obvious in the



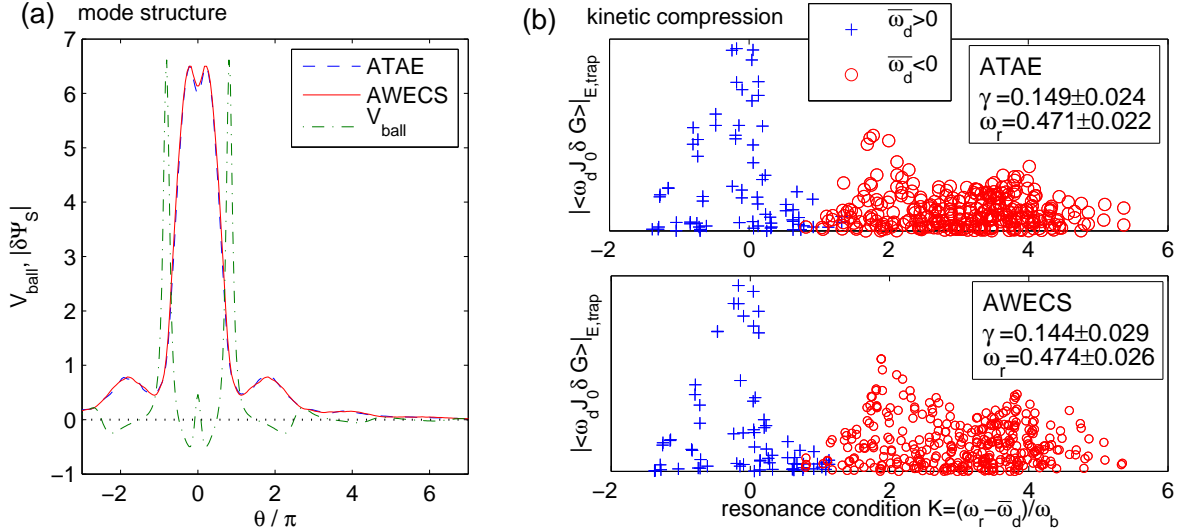


Figure 9: Benchmark of AWECs against ATAE for resonant excitation of  $\alpha$ TAEs by trapped energetic ions. In (a), the ballooning potential  $V_{\text{ball}}$  and the mode structure  $|\delta\Psi_s(\theta)| = \sqrt{f}|\delta\Psi_e(\theta)|$  are shown. In (b), the instantaneous contributions of individual phase-space markers to the kinetic compression term are plotted as a function of the resonance condition  $K = (\omega_r - \bar{\omega}_d)/\omega_b$ , distinguishing between particles with positive (+) and negative (reversed) precessional drift ( $\circ$ ). Most non-resonant particles are screened out in (b). The snapshot is taken at  $t = 400$  and the growth rates and frequencies are average values for  $t \in [320, 400]$ . The errors represent the standard deviation due to discretization noise; the uncertainty of the mean values is smaller than this noise level by a factor  $\sqrt{81} = 9$ .

AWECs data. For more accurate simulations in this regime, markers must be loaded in a broader range of the simulation domain. The size of the simulation domain itself may also need to be increased.

Near the second MHD ballooning stability boundary, in the range  $1.5 \lesssim \alpha \lesssim 1.6$ , the mode frequency  $\omega_r$  is similar to that of the 1st-order  $\alpha$ TAE obtained with the MHD shooting code,  $\omega_{\alpha\text{TAE}*}^{(1,0)}$ , as can be seen in Fig. 8(b). In the range  $1.6 \lesssim \alpha \lesssim 3$ , a 2nd-order  $\alpha$ TAE is excited. This mode is strongly damped for  $\alpha \lesssim 2.8$ , so shooting results for  $\omega_{\alpha\text{TAE}*}^{(2,0)}$  are available only for  $\alpha > 2.8$ . However, a  $\hat{k}_{0i}$ -scan at  $\alpha = 2.3$  revealed that  $\omega_r(\hat{k}_{0i} \rightarrow 0)$  is nonzero, which supports our assertion that the mode is an  $\alpha$ TAE.

In summary, the qualitative agreement between AWECs results and those by HZE94, and the agreement of the frequencies with those obtained for MHD  $\alpha$ TAEs suggests that AWECs accurately reproduces essential properties of high- $\beta$  shear-Alfvén instabilities. Discrepancies with results by DZCJ04 remain to be resolved. Further simulations using AWECs indicate that the effects of  $\delta B_{\parallel}$  and  $\Omega_p$  are small in the  $\alpha$  range scanned in the two cases discussed above. As an example, several points obtained using the full code are plotted in Fig. 8 (bold circles).

## 6 Benchmark 3: Resonant excitation of $\alpha$ TAEs by energetic ions

The excitation of  $\alpha$ TAEs through trapped energetic ions was previously demonstrated by Hu & Chen, 2005 (HC05) with the  $\delta f$  PIC code ATAE [28]. In this section, we use ATAE results as a benchmark for AWECs. ATAE employs a hybrid model consisting of an ideal-MHD core plasma (thermal electrons and ions) and a sparse population of trapped energetic ions. The dynamics of the latter is governed by the GKE (15). The equations are sufficiently simple to be advanced with a leap-frog scheme, which allows to solve the GKE directly, without the need to apply the substitution  $\delta G \rightarrow \delta g$ , Eq. (24).

In order to produce results comparable to those of ATAE, several adjustments needed to be carried out in AWECs:

- We omit all terms containing  $\lambda'_s$ ; i.e.,  $\delta S_2$  and  $\delta \Lambda_2$  and  $\langle v_{\parallel} \lambda' J_1 \delta G \rangle$ , which are neglected in ATAE.

- For the GKE, we adopt the  $\theta$ -dependence of  $\Omega_\kappa$ ,  $\Omega_p$  and  $\omega_{*s}$  as defined in ATAE, where these quantities are all  $\propto 1/\hat{B}$ .
- Let  $k_\perp \rho_{ci} \ll 1$ , take the ideal-MHD limit,  $\delta E_\parallel = 0$ , and approximate  $\omega \delta B_\parallel = -\Omega_p \delta \psi$ . In ATAE, we have replaced

$$\Omega_p = -(\mu_0/B^2) \mathbf{k}_\perp \cdot (\hat{\mathbf{b}} \times \nabla P_c),$$

where  $P_c = P - P_E$ , by

$$\Omega_p = -(\mu_0/B^2) \mathbf{k}_\perp \cdot (\hat{\mathbf{b}} \times \nabla P),$$

since the ordering  $\beta_E/\beta_c \sim \mathcal{O}(\varepsilon)$  used in Ref. [28] does not apply for the parameters used.

- We eliminate effects of passing energetic ions. For trapped energetic ions, we retain only the ballooning term and the kinetic compression.

The most important modifications are the neglect of thermal ion FLR effects, the parallel electric field and passing energetic ions. While the former two are easily implemented by setting  $\hat{k}_{0i} \ll 1$  and  $\delta U_e = 0$ , the latter requires careful adjustments. After the parallel Ampère's law is reduced to

$$\delta E_e \approx (1 - \Gamma_{0i}) \delta \Psi_e \approx b_i \delta \Psi_e,$$

we are left with the vorticity equation

$$\begin{aligned} f \hat{k}_{0i}^2 \partial_t^2 \delta \Psi_e = & \hat{k}_{0i}^2 [f \delta \Psi_e'' + 2hh' \delta \Psi_e'] + \frac{\tau_{Ei}^n}{\tau_{ei}} \langle \omega_d J_0 \delta G \rangle_{E, \text{trap}} \\ & + 4\omega_{*i} \Omega_{\kappa i} \delta \Psi_e + \hat{k}_{0i}^2 \alpha_{E, \text{pass}} g \delta \Psi_e + Z_E \tau_{Ei}^n \tau_{iE}^T \langle J_0^2 \omega_d \omega_*^T F_0 \rangle_{E, \text{trap}} \delta \Psi_e. \end{aligned} \quad (65)$$

The terms on the second line of Eq. (65) are components of the so-called ballooning term. Their drift-kinetic limit may be summarized as  $\hat{k}_{0i}^2 \alpha g \delta \Psi_e$  (not done here). The core component is

$$4\omega_{*i} \Omega_{\kappa i} = \hat{k}_{0i}^2 (\alpha - \alpha_E) g = \hat{k}_{0i}^2 \alpha_c g,$$

the contribution of passing energetic ions is  $\hat{k}_{0i}^2 \alpha_{E, \text{pass}} g$ , and that of the trapped energetic ions is contained in the term  $\langle J_0^2 \omega_d \omega_*^T F_0 \rangle_{E, \text{trap}}$ . The quantity  $\alpha_{E, \text{pass}}$  is calculated using the phase-space marker distribution for passing energetic ions at  $t = 0$ . Since the velocity space moment  $\langle \dots F_0 \rangle$  in Eq. (65) involves only trapped ions it needs to be evaluated numerically. Note that

$$f^{-1/2} (f \delta \Psi_e')' = \delta \Psi_s'' - V_{\text{ball}} \delta \Psi_s - \alpha (g/f) \delta \Psi_s$$

[cf. Eq. (63)], where the last term,  $\alpha (g/f) \delta \Psi_s$ , cancels with the drift-kinetic limit of the ballooning term.

In the benchmark simulation, the following parameters are used:

- Physical parameters:  $q = 2.0$ ,  $s = 0.5$ ,  $\alpha = 2.1$ ,  $\varepsilon_{nc} = \varepsilon_{nE} = 0.2$ ,  $v_{tE} = 0.7$ ,  $\hat{k}_{0E} = 0.21$ ,  $\tau_{ei}^T = 1.0$ ,  $\eta_c = 0.0$ ,  $\eta_E = 1.0$ ,  $\varepsilon = 0.2$ ,  $Z_E = M_E = 1$ . Some relevant parameters derived from the above are:  $\tau_{Ei}^n = 5 \times 10^{-2}$ ,  $\tau_{Ei}^T = 392$ ,  $\hat{k}_{0i} = 0.010606$ ,  $\beta_i = 2.5 \times 10^{-3}$ ,  $\alpha_E = 2.0$ ,  $\alpha_{E, \text{trap}} = 1.22$ .
- Numerical parameters:  $N_m = 512 \times 4 \times 3$ ,  $\theta_{\text{max}} = 60$ ,  $N_g = 1024$ ,  $\Delta t = 0.04$ . Since ATAE uses a 2nd-order leap-frog scheme the time step adjusted to  $\Delta t = 0.02$ .

This corresponds closely to the case shown in Fig. 1 of Ref. [28], with the difference that we use bounce angles in the range  $\theta_b \in [0.1^\circ, 179.9^\circ]$ .

The results are shown in Fig. 9. The mode structure in Fig. 9(a) shows an  $\alpha$ TAE with dominant (1,0) component. In Fig. 9(b), the instantaneous contributions of individual phase-space markers to the kinetic compression term are plotted as a function of the resonance condition  $K = (\omega_r - \bar{\omega}_d)/\omega_b$ , with  $\bar{\omega}_d$  being the bounce-averaged magnetic drift frequency and  $\omega_b$  the bounce frequency [13]. Resonances can be observed at even values of  $K$  which is consistent with the fact that  $\alpha$ TAE(1,0) is an eigenfunction with even parity. The precessional drift resonance,  $K = 0$ , is due to particles with  $\bar{\omega}_d > 0$ , whereas the drift-bounce resonances,  $K \geq 2$ , are due to particles with reversed drift  $\bar{\omega}_d < 0$ .

The good quantitative ( $\delta \Psi_e$ ,  $\omega_r$  and  $\gamma$ ) and qualitative (wave-particle resonance) agreement between results obtained with AWECS and ATAE shows that the interaction between trapped energetic ions and  $\alpha$ TAEs is accurately reproduced by AWECS with the reduced vorticity equation (65). Our preliminary studies indicate that the inclusion of thermal ion FLR effects,  $\delta E_\parallel \neq 0$  and passing energetic ions could significantly modify the results. To our knowledge, such a case has not been studied before and AWECS will be used to advance into this area.

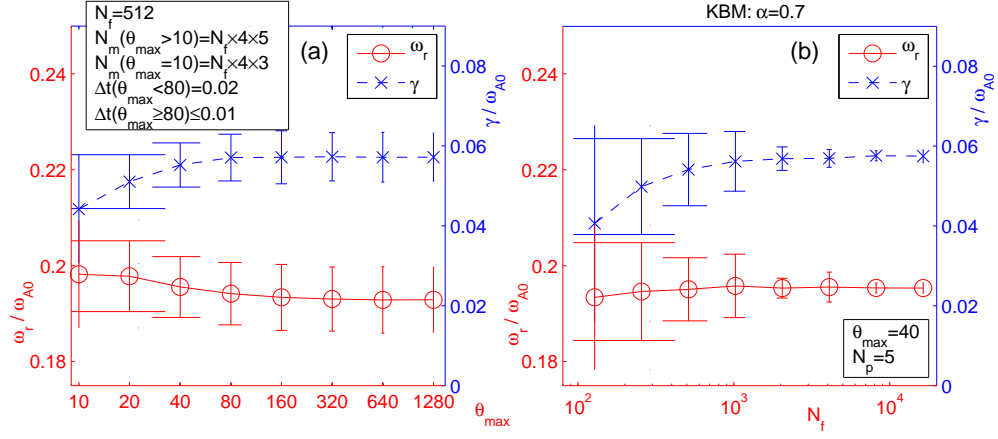


Figure 10: Convergence study for a case from Fig. 6 with  $\alpha = 0.7$  and  $\eta_i = 0$ ; i.e., a KBM without ITG-drive. (a) shows convergence with the simulation domain size  $\theta_{\max}$ , and (b) convergence with the number of markers  $N_m = N_{f,\text{ipass}} \times 4 \times N_p$  (controlled by  $N_{f,\text{ipass}}$ ).

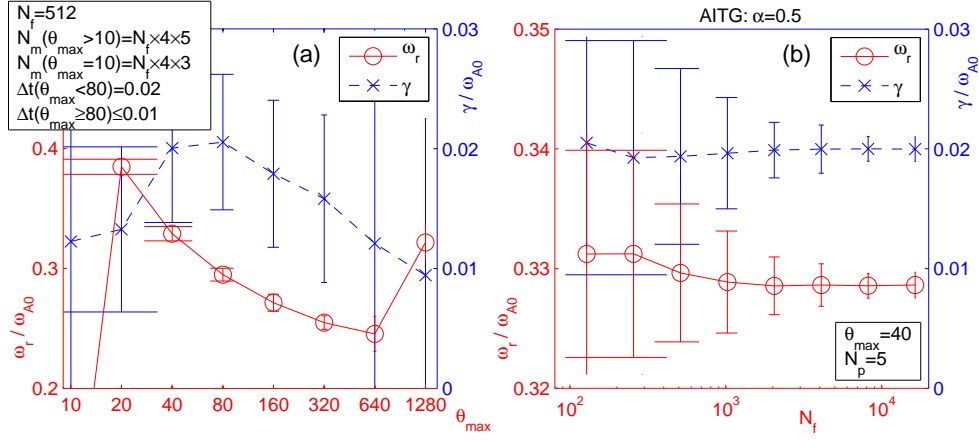


Figure 11: Convergence study for a case from Fig. 6 with  $\alpha = 0.5$  and  $\eta_i = 2.5$ ; i.e., at the instability threshold of AITG modes. (a) shows that convergence with the simulation domain size  $\theta_{\max}$  is not achieved. In (b), convergence with the number of markers  $N_m = N_{f,\text{ipass}} \times 4 \times N_p$  (controlled by  $N_{f,\text{ipass}}$ ) is demonstrated for a given domain size  $\theta_{\max} = 40$ .

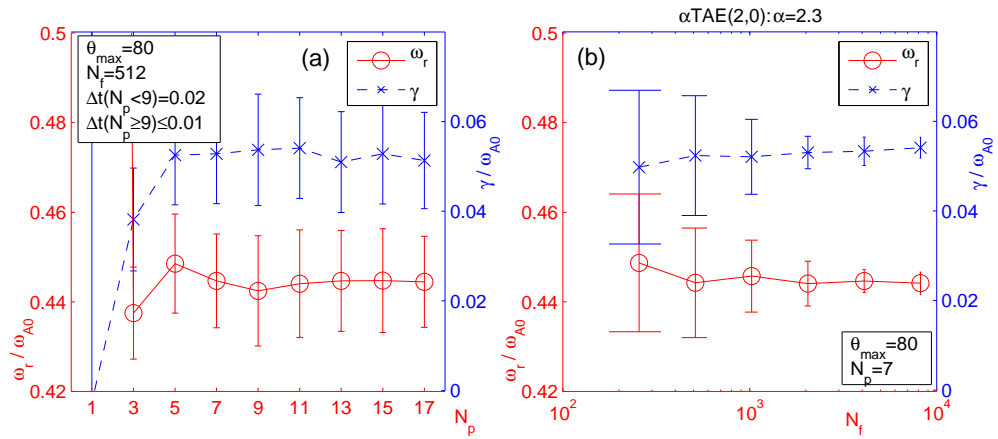


Figure 12: Convergence study for a case from Fig. 8 with  $\alpha = 2.3$  and  $\eta_i = 2.0$ ; i.e., a predominantly 2nd-order  $\alpha\text{TAE}$  driven by ITG. (a) shows convergence with the number of periods  $N_p$  in which markers are loaded, and (b) convergence with the number of markers  $N_m = N_{f,\text{ipass}} \times 4 \times N_p$  (controlled by  $N_{f,\text{ipass}}$ ).

## 7 Numerical convergence

Examples for numerical convergence with the domain size  $\theta_{\max}$ , the number of markers  $N_m = N_f \times 4 \times N_p$ , and the number of marker loading periods  $N_p$  are shown in Figs. 10, 11 and 12. The error bars indicate the level of discretization noise, which decreases with increasing number of markers. Only cases with  $\varepsilon = 0$  and without energetic ions are considered here; i.e.,  $N_p = N_{p,\text{ipass}}$  (passing thermal ions only).

In Fig. 10, a convergence study is shown for a KBM in the case considered by Dong *et al.*, 2004 (DCZJ04) [27] and Zhao & Chen, 2002 (ZC02) [25] (cf. Fig. 6). DCZJ04 used  $\theta_{\max} \approx 23$  and ZC02 used  $\theta_{\max} \leq 50 \dots 100$ , while Fig. 10(a) indicates that at least  $\theta_{\max} \sim 40$  is required in AWECS for numerical convergence. It is thus possible that the results by Dong *et al.* [26, 27] are not fully converged with respect to the simulation domain size. The AWECS results in Fig. 6 were obtained with  $N_m = 512 \times 4 \times 5$  markers, and the equivalent number of markers used in ZC02's calculations is  $N_m \approx (315 \dots 630) \times 4 \times 5$ , which appears to be sufficient according to Fig. 10(b).

Near the stability boundary, convergence with  $\theta_{\max}$  becomes problematic, as is illustrated in Fig. 11(a) for an AITG mode [25] (cf. Fig. 6). This result shows that it may be difficult to obtain an accurate value for  $\alpha_{\text{crit}}^{(\text{I})}$  (and possibly  $\alpha_{\text{crit}}^{(\text{II})}$ , as well) other than through extrapolation from converged results away from the stability boundary. Despite the lack of convergence with respect to  $\theta_{\max}$ , the results still converge well with the number of markers for a given  $\theta_{\max}$ , as can be seen in Fig. 11(b).

In Fig. 12, a convergence study is shown for higher-order  $\alpha$ TAEs (with dominant 2nd-order mode) in the 2nd stable domain in a case considered by Hirose *et al.*, 1994 (HZE94) [23]. Due to the broad mode structure, markers must be loaded in at least  $N_p = 7$  periods, as was done in Fig. 8 from which this case was taken. The number of markers was  $N_m = 512 \times 4 \times 7$ , which is also found to be sufficient.

Given the limitations of the model used, the accuracy of the results shown in Figs. 6–8 may be considered to be sufficient to delineate the qualitative features of the modes studied. For this purpose, it is usually not necessary to carry out the expensive calculations required for full convergence.

## 8 Conclusions and discussions

A 1-D linear gyrokinetic code called AWECS has been developed to study the kinetic excitation of Alfvénic instabilities in a high- $\beta$  tokamak plasma. The model equations and the numerical scheme are described and the code has been tested carefully. In particular, it is shown that AWECS reproduces successfully essential properties of ESITG and AITG modes, KBMs, and  $\alpha$ TAEs. Benchmarks against results in Refs. [16, 25, 19, 23, 28] are regarded as successful. However, discrepancies persist in comparisons with Refs. [26, 27].

While the real frequencies calculated by AWECS have also been confirmed by MHD shooting code calculations, the quantitative accuracy of the growth rates is more difficult to show, and it is here where the main discrepancy with Refs. [26, 27] lies. The code used by Zhao & Chen [25] is most directly comparable to AWECS (without energetic ions), and here the growth rates agree well. Numerical convergence studies in several typical cases indicate that accurate calculations require a larger simulation domain than used in Refs. [26, 27]. Furthermore, outgoing boundary conditions are required to accurately reproduce properties of modes subject to continuum damping, such as  $\alpha$ TAEs. Hence, the lack of numerical convergence and sensitivity to the boundary conditions may explain the discrepancies, as was previously suggested in Ref. [25].

Overall, it can be concluded that AWECS is functioning properly and that it can be used for further research. Since benchmarking cannot rule out all possible modeling and programming errors, AWECS will undergo continuing scrutiny while in operation. Code maintenance and extensions are simplified by the modular structure of the code and the application of principles of object-oriented programming. Interactive graphical tools were developed using MATLAB in order to assist the user in data analysis and post-processing tasks.

The demonstration of  $\alpha$ TAE excitation in the cases studied by Hirose *et al.*, 1994 [23] and Dong *et al.*, 2004 [27] constitutes the first successful application of this code. Note that, in these earlier works, the observed instabilities were not identified as  $\alpha$ TAEs, which were discovered more recently [7]. Details about the physics of  $\alpha$ TAE excitation through wave-particle interactions with thermal and

energetic ions will be reported elsewhere. With the use of AWECS, many other interesting problems may be addressed in the future, including the physics of BAEs, TAEs and EPMS.

In this paper, the CHT  $s$ - $\alpha$  model equilibrium is adopted in order to be able to carry out comparisons with previous studies, and, thereby, benchmark the code. Currently, work is underway to implement the local equilibrium model developed by Miller *et al.* [29] which will allow us to explore the high- $\beta$  regime more relevant to experiments. Further extensions are under consideration, such as the inclusion of effects due to magnetically trapped electrons.

Finally, two cautionary notes remain to be added. First, since the CHT  $s$ - $\alpha$  model is derived under the assumption that  $B$  is independent of  $\theta$ , there is a certain degree of arbitrariness in the way how the extension to a model with finite aspect ratio,  $\varepsilon > 0$  and, thus, variable  $B(\theta)$ , is carried out. Second, all velocity integrals not arising from the transformation  $\delta G \rightarrow \delta g$  must be evaluated analytically or using phase-space markers distributed uniformly along  $\theta$ . On the other hand, those integrals arising from the transformation  $\delta G \rightarrow \delta g$  must be evaluated numerically, utilizing the same markers used to calculate  $\delta g$  (nonuniform in  $\theta$ ). If this is not done, inconsistencies arise due to a mixing of  $\theta$ -independent and  $\theta$ -dependent densities. Preliminary tests where the ballooning term contains  $\hat{B}$ , so that the cancellation with the  $\alpha g/f$  term arising from the substitution  $\delta \Psi_e \rightarrow \delta \Psi_s$  [cf. Eq. (62) and the note following Eq. (65)] is incomplete, have shown that such inconsistencies may modify the ballooning potential to such a degree that unstable modes appear in the second MHD ballooning stable domain even without wave-particle interactions. In summary, care must be exercised when the CHT  $s$ - $\alpha$  model employed in this paper is used with finite aspect ratio,  $\varepsilon > 0$ .

## Acknowledgments

One of the authors (A.B.) would like to thank Z. Lin and Y. Nishimura (UCI), as well as F. Zonca (Euratom-ENEA, C.R. Frascati) for helpful discussions. The modular structure of AWECS was partly inspired by a PIC framework developed at UCLA by V. Decyk and C. Norton. Further ideas, in particular with regard to parallelization using MPI, were adopted from the code D3D by B. Scott (Max-Planck-IPP Garching). This research is supported by U.S. DoE Grant DE-AC02-CH0-3073, NSF Grant ATM-0335279, and in part by SciDAC GSEP.

## Erratum

In the published version of this work [A. Bierwage & L. Chen, *Communication of Computational Physics* **4**, 457 (2008)], the following errors were found:

1. The coefficient in front of  $\delta U_e$  on the left-hand side of Eq. (2.33) was  $(1/\tau_{ei}^T + \Gamma_{0i} - H_\omega)$  but should read

$$\left[1/\tau_{ei}^T + \Gamma_{0i} - (H_\omega - Z_E \tau_{Ei}^n \tau_{iE}^T)\right]. \quad (66)$$

2. The coefficient in front of  $\delta C_e$  on the left-hand side of Eq. (2.36) was  $(\hat{B}^2 + A_\Sigma^2 A_\omega)$  but should read

$$(\hat{B}^2 + \mathcal{T}_i A_\Sigma^2 A_\omega). \quad (67)$$

3. The title of Section 4.2 was “Zero aspect ratio” but should read “Zero inverse aspect ratio.”

## References

- [1] K.-L. Wong, Plasma Phys. Control. Fusion **41**, R1 (1999).
- [2] F. Romanelli, Phys. Fluids B **1**, 1018 (1989).
- [3] F. Zonca, L. Chen, R. A. Santoro, and J. Q. Dong, Plasma Phys. Control. Fusion **40**, 2009 (1998).
- [4] S.-T. Tsai and L. Chen, Phys. Fluids B **5**, 3284 (1993).
- [5] M. Chu, J. Greene, L. Lao, A. Turnbull, and M. S. Chance, Phys. Fluids B **4**, 3713 (1992).
- [6] C. Cheng, L. Chen, and M. Chance, Ann. Physics **161**, 21 (1985).
- [7] S. Hu and L. Chen, Phys. Plasmas **11**, 1 (2004).
- [8] L. Chen, Phys. Plasmas **1**, 1519 (1994).
- [9] A. B. Mikhailovskii, *Theory of Plasma Instabilities* (Consultants Bureau, New York, 1974).
- [10] F. Zonca and L. Chen, Plasma Phys. Control. Fusion **48**, 537 (2006).
- [11] J. T. M. Antonsen and B. Lane, Phys. Fluids **23**, 1205 (1980).
- [12] J. W. Connor, R. J. Hastie, and J. B. Taylor, Phys. Rev. Lett. **40**, 396 (1978).
- [13] L. Chen and A. Hasegawa, J. Geophys. Res. **96**, 1503 (1991).
- [14] S. Dettrick, L.-J. Zheng, and L. Chen, J. Geophys. Res. **108**, 2250 (2003).
- [15] M. Abramowitz and I. A. Stegun, eds., *Handbook of Mathematical Functions* (Dover, New York, 1972), section 25.5, p. 896.
- [16] J. Q. Dong, W. Horton, and J. Y. Kim, Phys. Fluids B **4**, 1867 (1992).
- [17] G. Zhao, Ph.D. thesis, Department of Physics and Astronomy, University of California, 4129 Frederick Reines Hall, Irvine, CA, 92612, USA (2001).
- [18] GS2 Homepage: <http://gs2.sourceforge.net/>.
- [19] Y. Idomura, S. Tokuda, and Y. Kishimoto, J. Plasma Fusion Res. SERIES **6**, 17 (2004).
- [20] A. M. Dimits, G. Bateman, M. A. Beer, B. I. Cohen, W. Dorland, G. W. Hammett, C. Kim, J. E. Kinsey, M. Kotschenreuther, A. H. Kritz, et al., Phys. Plasmas **7**, 969 (2000).
- [21] W. M. Tang, J. W. Connor, and R. B. White, Nucl. Fusion **21**, 891 (1981).
- [22] L. Chen, A. Bondeson, and M. S. Chance, Nucl. Fusion **27**, 1918 (1987).
- [23] A. Hirose, L. Zhang, and M. Elia, Phys. Rev. Lett. **72**, 3993 (1994).
- [24] A. Hirose, L. Zhang, and M. Elia, Phys. Plasmas **2**, 859 (1995).
- [25] G. Zhao and L. Chen, Phys. Plasmas **9**, 861 (2002).
- [26] J. Q. Dong, L. Chen, and F. Zonca, Nucl. Fusion **39**, 1041 (1999).
- [27] J. Q. Dong, L. Chen, F. Zonca, and G. D. Jian, Phys. Plasmas **11**, 997 (2004).
- [28] S. Hu and L. Chen, Plasma Phys. Control. Fusion **47**, 1251 (2005).
- [29] R. L. Miller, M. S. Chu, J. M. Greene, Y. R. Lin-Liu, and R. E. Waltz, Phys. Plasmas **5**, 973 (1998).
- [30] R. D. Hazeltine and J. D. Meiss, Phys. Reports **121**, 1 (1985).